

Investigating the eccentricity distribution of transiting, long-period giant planets

Ahlam Alqasim ^{1,2}★, Teruyuki Hirano ^{2,3}, Yasunori Hori ^{2,3}, Daisuke Kawata ^{1,3},
John Livingston ^{2,3,4}, Steve B. Howell ⁵, Antonino F. Lanza ⁶, Andrew W. Mann ⁷, Carl Ziegler ⁸,
César Briceño,⁹ Charles A. Beichman ¹⁰, David R. Ciardi ¹¹, Ivan A. Strakhov ¹², Michael
B. Lund ¹¹ and Nicholas Law⁷

¹UCL Mullard Space Science Laboratory, Holmbury Hill Road, Dorking, Surrey RH5 6NT, UK

²Astrobiology Center, 2-21-1 Osawa, Mitaka, Tokyo 181-8588, Japan

³National Astronomical Observatory of Japan, 2-21-1 Osawa, Mitaka, Tokyo 181-8588, Japan

⁴Department of Astronomical Science, The Graduate University for Advanced Studies, 2-21-1 Osawa, Mitaka, Tokyo 181-8588, Japan

⁵NASA Ames Research Center, Moffett Field, CA 94035, USA

⁶INAF-Osservatorio Astrofisico di Catania, Via S. Sofia, 78 - 95123 Catania, Italy

⁷Department of Physics and Astronomy, The University of North Carolina at Chapel Hill, Chapel Hill, NC 27599-3255, USA

⁸Department of Physics, Engineering and Astronomy, Stephen F. Austin State University, 1936 North St, Nacogdoches, TX 75962, USA

⁹Cerro Tololo Inter-American Observatory, Casilla 603, La Serena, Chile

¹⁰NASA Exoplanet Science Institute-Caltech/IPAC and Jet Propulsion Laboratory, Pasadena, CA 91125, USA

¹¹NASA Exoplanet Science Institute-Caltech/IPAC, 1200 E. California Blvd, Pasadena, CA 91125, USA

¹²Sternberg Astronomical Institute, Moscow State University, Universitetski pr., 13, Moscow 119992, Russia

Accepted 2025 March 6. Received 2025 February 23; in original form 2024 December 29

ABSTRACT

Eccentric giant planets are predicted to have acquired their eccentricity through two major mechanisms: the Kozai–Lidov effect or planet–planet scattering, but it is normally difficult to separate the two mechanisms and determine the true eccentricity origin for a given system. In this work, we focus on a sample of 92 transiting, long-period giant planets (TLGs) as part of an eccentricity distribution study for this planet population in order to understand their eccentricity origin. Using archival high-contrast imaging observations, public stellar catalogs, precise *Gaia* astrometry, and the NASA Exoplanet Archive data base, we explored the eccentricity distribution correlation with different planet and host-star properties of our sample. We also homogeneously characterized the basic stellar properties for all 86 host-stars in our sample, including stellar age and metallicity. We found a correlation between eccentricity and stellar metallicity, where lower-metallicity stars ($[\text{Fe}/\text{H}] \leq 0.1$) did not host any planets beyond $e > 0.4$, while higher-metallicity stars hosted planets across the entire eccentricity range. Interestingly, we found no correlation between the eccentricity distribution and the presence of stellar companions, indicating that planet–planet scattering is likely a more dominant mechanism than the Kozai–Lidov effect for TLGs. This is further supported by an anticorrelation trend found between planet multiplicity and eccentricity, as well as a lack of strong tidal dissipation effects for planets in our sample, which favour planet–planet scattering scenarios for the eccentricity origin.

Key words: methods: statistical–planets and satellites: gaseous planets–planet–star interactions–stars: fundamental parameters.

1 INTRODUCTION

Giant exoplanets have been suggested to have a significant effect on the formation and evolution of planetary systems (Levison & Agnor 2003; Childs et al. 2019). Eccentric giant planets could have acquired their eccentricity through two major mechanisms: the Kozai–Lidov effect (Fabrycky & Tremaine 2007) or planet–planet scattering (Naoz et al. 2011). However, it is often difficult

to differentiate between the two mechanisms for any single system (Jurić & Tremaine 2008). Even methods such as the Rossiter–McLaughlin effect do not help much in distinguishing between these two scenarios (Beaugé & Nesvorný 2012). Up to a few M_{Jup} , eccentric planets are expected to have evolved via planet–planet scattering (Bitsch, Trifonov & Izidoro 2020). Additionally, planet scattering followed by interactions with outer planets can also excite planets to high eccentricities (Nagasawa & Ida 2011). In contrast, Nagasawa, Ida & Bessho (2008) found that the Kozai–Lidov mechanism in outer planets can cause the formation and eccentricity excitation of close-in planets. This is also in agreement with the findings of Bonomo et al.

* E-mail: ahlam.alqasim.17@ucl.ac.uk

(2017) for transiting hot Jupiters, who found that those planets are consistent with formation through high-eccentricity migration. Thus, inner planets with moderate eccentricities could have evolved via this mechanism without the presence of any close-in companions. Giant planets have been predicted to be more likely found in multiplanet systems (Bitsch et al. 2020). Ida, Lin & Nagasawa (2013) showed that distant giant companions could be formed with nearly circular orbits via scattered residual cores from emerging gas giants. A population study on a statistical level for the observed distribution of such planets could provide better insights into their eccentricity origins and evolution history.

Eccentricity distributions of transiting close-in giant planets (namely, Hot Jupiters) have been extensively studied (Knutson et al. 2014; Bonomo et al. 2017), with many follow-up campaigns to try to search for predicted long-period companions (Ngo et al. 2016). However, the eccentricity distributions of more distant giant planets (e.g. warmer and longer-period Jupiter, Saturn, and Neptune-like exoplanets) have not been well studied, and their eccentricity and formation pathways tend to differ from Hot Jupiters, which makes them all the more important to explore. Thus, investigating the planet eccentricity correlations of distant giant planets on a statistical level would enable us to validate whether different theoretical predictions reflect the observed planet distribution and their system properties. It would also enable us to probe which mechanism could be responsible for the eccentricity origin of planets in our sample. The analysis presented in this paper is distinct and new in comparison to previous works, given that we are only focusing on transiting, long-period giant planets.

Our motivation is to (1) investigate the correlation of different planet and stellar properties with the eccentricity distribution for our sample of long-period exoplanets, and (2) try to distinguish between different evolution scenarios (e.g. Kozai–Lidov effect, planet–planet scattering, etc.) that could have caused planets in our sample to become eccentric. Our population study utilizes archival high-contrast imaging observations, public stellar catalogs, precise *Gaia* astrometry, and the NASA Exoplanet Archive data base, to enable us to better understand and probe the origin of the eccentricity for our target sample.

Our paper is structured as follows: in Section 2, we describe the criteria used to select our sample. Section 3 describes the homogeneous characterization of the basic stellar properties for our host-stars. In Section 4, we describe the internal composition modelling performed for the planets in our sample. Section 5 details how we construct our eccentricity distributions and measure their significance in comparison with different properties. We present our results and discuss the implications of our findings in Section 6, and any possible biases of the study in Section 7. We end with the summary and conclusions in Section 8.

2 SAMPLE SELECTION

The focus of our investigation is on transiting, long-period giant planets (henceforth referred to as TLGs), which are less vulnerable to tidal circularization. As such, we selected a planet sample with a minimum mass of $10 M_{\oplus}$ and with orbital periods of $P > 10$ d. We place this minimum mass constraint to avoid biases on the lower eccentricity, since the eccentricity measurements are not as reliable below $10 M_{\oplus}$ and are often set to 0. We also placed the requirement that planets in our sample are transiting and have been observed with radial velocity instruments. We limited our sample to transiting systems to ensure that we have a radius measurement of the planet, enabling us to utilize the planet density in our study when combined

with the mass measurements from radial velocities. We required that all planets in our sample had reported error measurements for radius, mass and eccentricity to ensure the reliability of the results, in particular with regards to eccentricity.

We extracted our target sample from the NASA Exoplanet Archive¹ (Akeson et al. 2013) (henceforth referred to as NEXA), as of 2024 May 9. We use the Planetary Systems Composite Parameters (PSCompPars) table, which provides a more statistical view of the known exoplanet population and their host environments according to NEXA. We queried the table using NEXA’s TAP service.² We summarize the criteria used for our sample selection as follows:

(i) Error requirement: The error measurements of the planet radius, mass, period, and eccentricity are available (non-null). This is filtered using the upper error bound columns.

(ii) Mass cut: $M_p > 10 M_{\oplus}$

(iii) Period cut: $P > 10$ d

(iv) Transit flag: `tran_flag = 1`

(v) Radial velocity flag: `rv_flag = 1`

(vi) Metallicity flag: `st_metratio = [Fe/H]`

(vii) Discovery method: `discoverymethod = ‘Radial Velocity’` or `‘Transit’`

Our sample is comprised of 86 target stars hosting a total of 92 exoplanets, 41 per cent of which are eccentric (using $e = 0.2$ as the cut off between higher and lower eccentricity systems). Fig. 1 shows the radius, mass and period versus eccentricity for the full target sample. The Radius–Eccentricity plot in the figure shows a separation of our planet sample into two populations around $\sim 6 R_{\oplus}$, while the Period–Eccentricity plot shows a lack of planets at lower eccentricities ($e \leq 0.2$) past $P \sim 150$ d. Since part of our study explores the eccentricity dependency on the presence of stellar companions (see Section 6.2), the availability of high resolution imaging observations plays a significant role in those findings. Only 7 out of the 86 host stars in our sample are lacking imaging data (~ 8 per cent), which are highlighted in grey in the figure. We are currently in the process of acquiring high resolution imaging (speckle or adaptive-optics observations) for these targets over the next couple of observing semesters for the purpose of completeness.

Appendix A includes tables of NEXA-derived parameters of our target list that were used in our study. Table A1 summarizes the planet parameters extracted from NEXA for our sample, and Table A2 summarizes the stellar parameters of the host stars in our sample. The reported error bars in the tables correspond to the mean uncertainty of the upper and lower error bounds of the parameters.

For targets missing ages in our sample, we manually checked the publication source to see whether they were available in the literature but were somehow missed by NEXA. We found a published age of 4 ± 1 Gyr in the literature for TOI-4582 (TIC 219854519), which we manually added to our table. Some targets – HAT-P-17 (TIC 266593143), WASP-117 (TIC 166739520), HD 17 156 (TIC 302773669), HAT-P-15 (TIC 353459965), Kepler-413 (TIC 298969838), and HD 80 606 (TIC 457134360) – were missing stellar metallicity ([Fe/H]) uncertainties in the queried NEXA table, but were found to be available online on the NEXA website and were somehow not getting picked up by the query. As such, we manually added the missing information to our table. Kepler-413 (TIC 298969838) was also missing the stellar effective temperature ($T_{\text{eff},*}$) uncertainty from the queried table despite being available

¹<https://exoplanetarchive.ipac.caltech.edu>

²<https://exoplanetarchive.ipac.caltech.edu/docs/TAP/usingTAP.html>

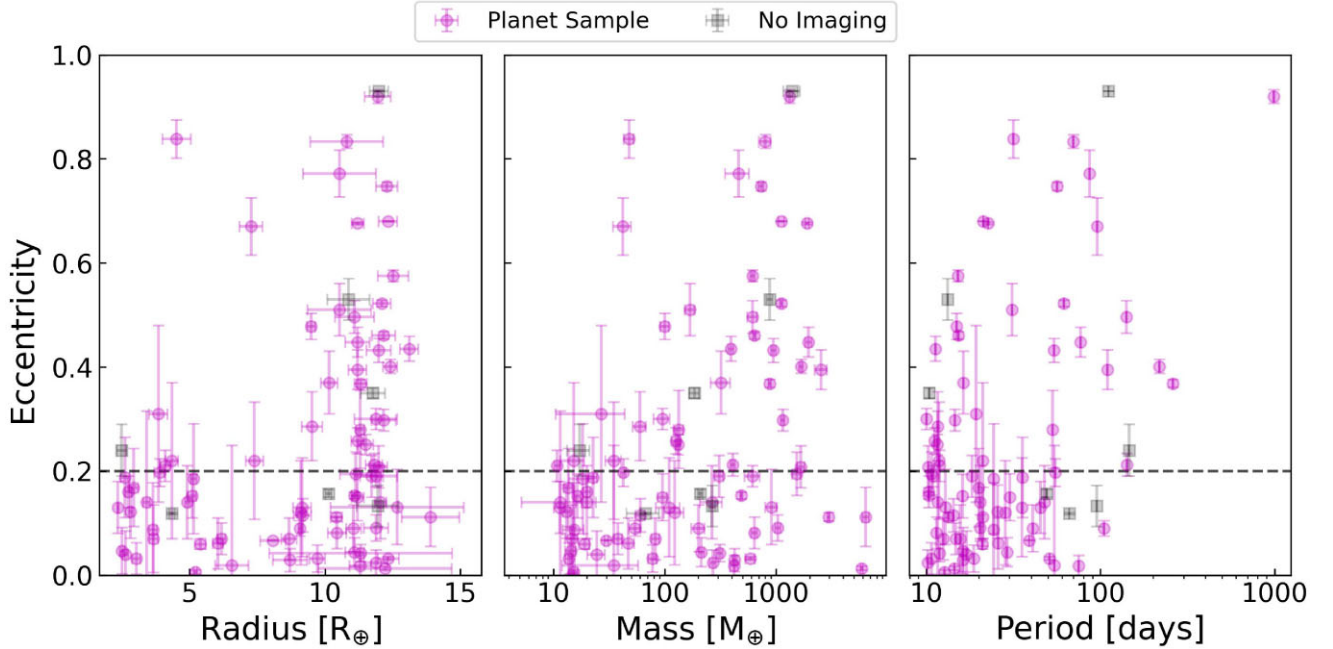


Figure 1. Radius, Mass, and Period versus Eccentricity (from left to right, respectively) for our target sample. Planets that are part of systems missing high-contrast imaging observations are coloured in grey squares.

online on NEXA, so we manually updated our table to include it accordingly.

All planet parameters used in this study were taken from our queried NEXA sample described in this section, unless otherwise mentioned. The NEXA stellar parameters were only used as priors for our homogeneous characterization of the host stars in our sample (see Section 3).

3 STELLAR CHARACTERIZATION

We homogeneously characterize the general stellar properties of our 86 host stars using JAXSTAR,³ a PYTHON module that provides fast isochrone fitting using HMC-NUTS. The method of isochrone fitting was validated using injection-and-recovery tests as well as tests using Kepler seismic stars, which have precise and accurate parameter constraints from asteroseismology (see Masuda 2022, for more details).

To run JAXSTAR, we used the queried NEXA values and their corresponding errors (see Table A2) for the stellar effective temperature $T_{\text{eff},*}$, metallicity [Fe/H], and K magnitude as priors for the fit, in addition to the precise parallax measurements of our targets from the *Gaia* DR3 catalog. One system, Kepler-413 (TIC 298969838, highlighted in blue in Fig. B2), had a reported metallicity value of -1.44 ± 0.3 on NEXA, which is unrealistic for an exoplanet host star and is probably a result of a technical error. As such, we instead use the stellar metallicity [M/H] and $T_{\text{eff},*}$ from the *Gaia* DR3 catalog (Gaia Collaboration 2023) as priors for this target. The reported values for [M/H] and $T_{\text{eff},*}$ from *Gaia* DR3 for this source are -0.39 ± 0.03 and 4875_{-18}^{+22} K, respectively. For the error bar used in the prior, we took the mean value of the upper and lower error bounds. Finally, we ran the HMC fit for 20 000 warm-up steps and 20 000 samples for each host star.

Appendix B includes tables and figures related to JAXSTAR-derived parameters of the host stars in our sample. Figs B1 and B2 show the comparison between the NEXA versus JAXSTAR-derived stellar ages and metallicities, respectively. Fig. B3 shows the mass distribution of our sample of host stars. Our homogeneously derived stellar parameters from JAXSTAR are available in Table B1. Four systems—TOI-1278 (TIC 163539739), K2-10 (TIC 363573185), TOI-1231 (TIC 447061717), and Kepler-413 (TIC 298969838) – do not have any reported stellar ages in NEXA or in the literature, and we present their newly-derived JAXSTAR ages in the table as well. We achieve a better mean error precision for the stellar ages by ~ 4 per cent, with the JAXSTAR mean error being 1.76 Gyr compared to the NEXA mean error of 1.83 Gyr. Similarly, we achieve a better mean error precision for the stellar metallicities [Fe/H] by ~ 11 per cent, with the JAXSTAR mean error being 0.056 compared to the NEXA mean error of 0.063.

In our analyses for this study, we use our homogeneous JAXSTAR-derived stellar parameters wherever relevant or necessary.

4 INTERNAL PLANET COMPOSITION

Considering three types of planetary materials (i.e. rock, water ice, and H/He gas), we simulated the interior structures of the planets in our sample using the planet mass, radius and equilibrium temperature. We used the planetary equilibrium temperature assuming zero Bond albedos. The interior structure of the planet is integrated using four equations of states (EoS): the Birch–Murnaghan EoS and the Thomas–Fermi Dirac EoS at $P > 1.35 \times 10^4$ GPa of MgSiO₃ for rock (Seager et al. 2007), AQUA EoS for water ice (Haldemann et al. 2020), and H/He (Chabrier & Debras 2021). We found that our sample of planets can be categorized by the following 5 groups based on their internal composition (see Fig. 2):

- (i) Gas giant planets ($R_p > 8 R_{\oplus}$ and $M_p > 50\text{--}60 M_{\oplus}$)
- (ii) Mini-gas giant planets ($R_p > 6 R_{\oplus}$ and $M_p \sim 30\text{--}50 M_{\oplus}$)

³<https://github.com/kemasuda/jaxstar>

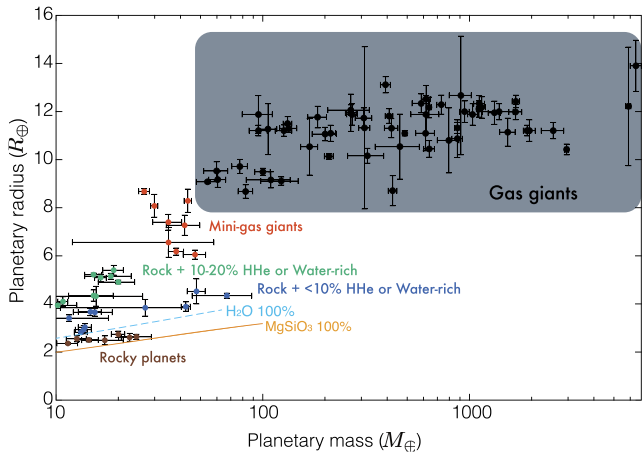


Figure 2. Mass–radius diagram of our planet sample. Theoretical interior models of pure water planets and pure rocky planets are shown as dashed lines and solid lines, respectively.

- (iii) Rocky planets with 10–20 per cent H/He envelope or Water-rich planets ($R_p > 4 R_\oplus$ and $M_p \sim 10\text{--}20 M_\oplus$)
- (iv) Rocky planets with < 10 per cent H/He envelope or Water-rich planets ($R_p \sim 3\text{--}4 R_\oplus$)
- (v) Rocky planets with < a few per cent H/He ($R_p < 3 R_\oplus$)

Note that the mass–radius relation of small planets allows two solutions for their internal composition: water-rich planets and rocky planets surrounded by H/He envelopes. We use these five groups to help us parametrize the modified tidal quality factor Q_p in Section 6.6.2 when calculating the tidal dissipation time-scale.

5 ECCENTRICITY DISTRIBUTION

In this paper, we explore the eccentricity distribution of TLGs and investigate their correlation with different planetary and stellar factors, which could provide useful insights into the eccentricity origin of our planet sample. We use the eccentricity measurements queried from NEXA, as described in Section 2. Fig. 3 shows the eccentricity distribution of all 92 planets in our target list. In the following sections, we divide our sample based on different criteria to see whether the inherent eccentricity distribution is dependent on

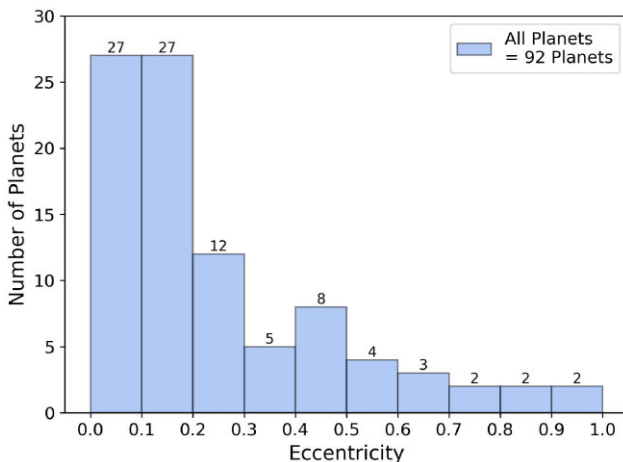


Figure 3. Eccentricity distribution of all 92 planets in our sample.

such factors. More specifically, we test the eccentricity correlation of TLGs with: stellar age, stellar companion, planet radius, planet multiplicity, planet equilibrium temperature, planet tidal dissipation time-scale (in relation to stellar age), and stellar metallicity.

To test the significance of our eccentricity distributions across different parameter spaces, we perform the Kolmogorov–Smirnov (K–S) test using the built-in `kstest` function from the `SCIPY PYTHON` module (Virtanen et al. 2020). This enables us to compare sub-samples of the eccentricity distribution according to different cuts and test the null hypothesis for whether they are distributed according to the standard normal. We discuss the selection criteria used to split our sample and perform the K–S tests in each subsequent section separately, along with the implications of our results. Additionally, we use the Spearman correlation coefficient (also known as the Spearman ρ test) to verify the existence of a correlation between two continuous parameters that are not split by categories. We use the built-in `spearmanr` function from the `SCIPY PYTHON` module (Virtanen et al. 2020). Since this is a non-parametric test, it does not make assumptions on the specific form of the correlation, and allows us to analytically calculate the probability that a given value of the Spearman coefficient comes by chance when there is no correlation. While the p -value calculation in this test does not make strong assumptions about the distributions underlying the samples, it is only accurate for very large samples (>500 observations). For smaller samples, it is more appropriate to perform a permutation test, where one can produce an exact null distribution by calculating the statistic under each possible pairing of elements between the two continuous parameters. Since our sample is small and consists of 92 planets, we perform a permutation test when calculating the p -value for the Spearman ρ test.

For continuous parameters, the K–S test requires us to fix a boundary value for one of the two variables to construct the two distributions to be compared. Since this choice is not unique in most cases, we chose to perform Spearman ρ tests when both variables are continuously varying. On the other hand, the K–S method is very useful and appropriate when there is a natural way to define different distributions to be compared based on categories (e.g. stars with detected distant companions and star without detected companions). Using a confidence level of 95 per cent, we consider a parameter to be statistically significant when tested for correlations with eccentricity if both the K–S test and the Spearman ρ test have p -values less than 0.05 (when the parameter is not continuous, we only consider the K–S test).

6 RESULTS AND DISCUSSION

In this work, we focused on a sample of 92 transiting, long-period giant planets as part of an eccentricity distribution study for this planet population in order to understand their eccentricity origin. Our main focus in the present paper is to look for trends and possible correlations in the eccentricity distribution, and the detailed comparisons with theoretical models/expectations will be given in future works. Past studies have performed population level analyses for the eccentricity distributions of small planets (Kane et al. 2012; Xie et al. 2016; Van Eylen et al. 2019) and close-in giant planets (Knutson et al. 2014; Bonomo et al. 2017), but long-period giant planets remain widely unexplored. In particular, previous studies of giant planets focused on hot Jupiters, which are substantially different to TLGs and have different characteristics and formation pathways. As such, direct comparisons are difficult to make in our specific case since the eccentricity distributions of TLGs have not

Table 1. Results of the statistical tests used to determine which parameters are correlated with eccentricity. The thresholds listed are only used for the K–S tests, since the sample had to be split based on a cut-off threshold in order to compare the two distributions. Parameters with no listed thresholds were divided by category (e.g. companion versus no companion, single versus multi). They were also not tested under the Spearman ρ Test since they are not continuous parameters. p -values that were found to be <0.05 are highlighted in bold.

Parameter Name	Threshold	p -value (K–S Test)	p -value (Spearman ρ Test)
Stellar Age [Gyr]	5	0.930	0.442
Stellar Metallicity [Fe/H]	0.1	0.022	0.040
Stellar Companion	–	0.956	–
Stellar Effective Temperature T_{eff} [K]	5629	0.494	0.250
Planet Period [days]	21	0.211	0.070
Planet Radius R_p [R_{\oplus}]	6	0.030	0.005
Planet Multiplicity N	–	0.048	–
Planet Equilibrium Temperature T_{eq} [K]	500	0.973	0.676
Time-scale Ratio τ ($Q_p = 10^2$)	0.9	0.035	0.089
Time-scale Ratio τ ($Q_p = 10^3$)	0.9	0.279	0.089
Time-scale Ratio τ ($Q_p = 10^4$)	0.9	0.669	0.089
Time-scale Ratio τ ($Q_p = 10^5$)	0.9	0.316	0.089
Time-scale Ratio τ (Varying Q_p)	0.9	0.310	0.018

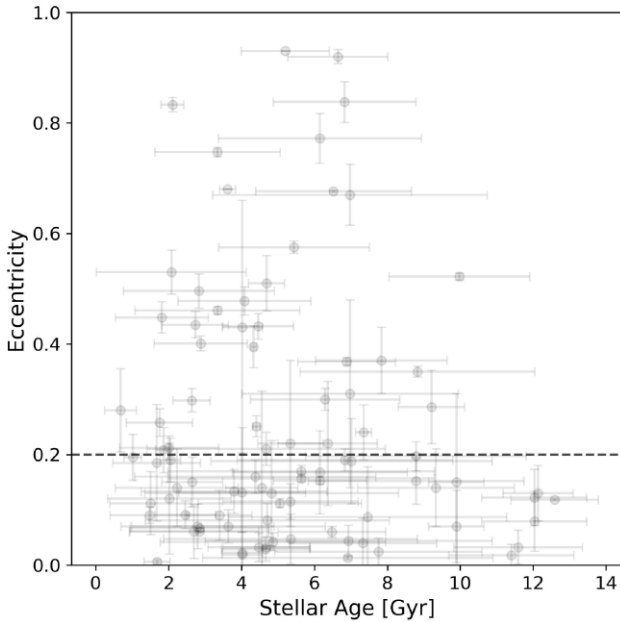


Figure 4. Stellar Age versus Eccentricity for all 92 planets in our sample.

been well explored before, but we highlight any relevant comparisons that could be made when possible.

In the following subsections, we present our findings of the eccentricity distributions in relation to stellar age, stellar companion, planet radius, planet multiplicity, planet equilibrium temperature, tidal dissipation, and stellar metallicity. We then discuss the implications of our findings for each correlation (or lack of) with the eccentricity distribution of TLGs. The results of the parameters tested for statistical correlations against eccentricity are presented in Table 1.

6.1 Stellar age

We explore the stellar age correlation to the planet eccentricity for our sample of TLGs. Fig. 4 shows the stellar age versus eccentricity for all 92 planets in our sample. There are no visible trends or correlations by eye, and the ages appear to be distributed relatively homogeneously.

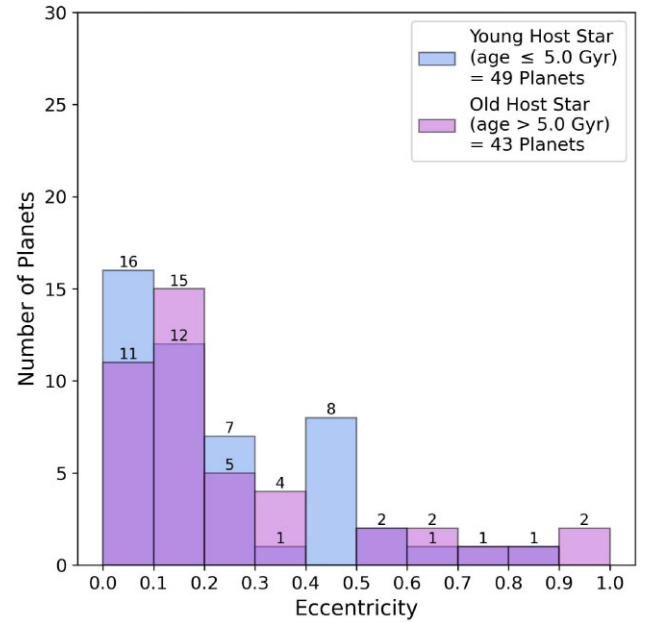


Figure 5. Eccentricity distribution of planet systems with young (blue) versus old (magenta) host stars in our sample, using 5 Gyr as the cut-off threshold between the two sub-samples.

Although, we note a lack of high- e planets around older host-stars (Age > 10 Gyr), which could suggest that these planetary systems have settled down.

To check for statistical correlations using the K–S test, we split our sample based on whether planets belong to young or old host-stars, using 5 Gyr as the cut-off threshold between the two sub-samples. This threshold was chosen based on the median age of our sample. Fig. 5 shows the eccentricity distribution of planet systems with young (blue) versus old (magenta) host stars in our sample. Both results from the K–S test and the Spearman ρ test have p -values > 0.05 , indicating that there is no statistical correlation between age and eccentricity.

The lack of correlation between host-star age and planet eccentricity for our sample TLGs is not surprising. Previous studies of eccentricity distributions do not report any correlation with stellar

age, even across planet groups beyond TLGs (Udry & Santos 2007; Bowler, Blunt & Nielsen 2020). Interestingly, we only find young host-star planets in the 0.4–0.5 eccentricity bin in Fig. 5, but the lack of old host-star systems in this regime is likely a result of the small sample size beyond $e > 0.2$, whereas the sample size for young host-star planets only starts to decrease significantly beyond $e > 0.4$. Thus, we cannot determine whether this observation is to be attributed to a sampling issue or has a physical explanation related to the host-star age.

Swastik et al. (2023) determined the age distribution of exoplanet host-stars and found that stars hosting giant planets tend to be younger than stars hosting small planets, but the study did not explore whether there was any correlation with the planet eccentricity. We also note that stellar ages are generally difficult to estimate and usually have very large error bars. While we managed to derive homogeneous measurements of stellar ages and achieved better error precisions than the ages reported on NEXA, there are still issues with model degeneracies when performing isochrone fitting. Other methods of determining ages (such as astroseismology) have been shown to provide more accurate measurements (Silva Aguirre et al. 2015; Aerts 2021), but astroseismic data are limited, making it difficult to utilize in statistical studies without compromising on the sample size.

In younger systems, planets can form with a diverse range of eccentricities, and can start off with very high eccentricities due to the chaotic interactions and processes during the early stages of formation. As the system stabilizes with time and age, such planets (especially ones that formed or migrated close to the host star) will have undergone tidal dissipation and began to circularize, causing eccentricities to be dampened to lower values over time (Villaver et al. 2014). So, as the system reaches older ages, we would expect to see fewer planets with very high eccentricities. In our case, given the period cut we placed at 10 d, the planets in our sample are too far from the host star for tidal dissipation effects to cause any significant eccentricity damping. As a sanity check, we tested whether there was any period correlation with eccentricity given the period cut we imposed. Both results from the K–S test and the Spearman ρ test have p -values > 0.05 , indicating that there is no statistical correlation between period and eccentricity. As such, we do not expect age to play a significant role on the observed eccentricity in our planet sample, which is also confirmed by our findings. A more detailed discussion on the effects of tidal dissipation for our sample can be found in Section 6.6.

6.2 Stellar companion

We explore the correlation between the presence of stellar companions to the planet eccentricity for our sample of TLGs.

To find systems with a nearby stellar companion, we manually searched the Exoplanet Follow-up Observing Program (ExoFOP) website⁴ for each target and checked whether high-resolution imaging observations were taken, and if so, whether there was any evidence of detected companions reported. We placed no constraints on the separation of the companion, and we caution that this approach depends on the detection limits of the instrument and telescope used, which is heterogeneous across our sample. On ExoFOP, our targets had Speckle, AO or Lucky imaging, and in some cases, they were observed by more than one imaging technique. Some of the AO imaging observations used in this study will be published as part of a catalogue paper by Dressing et al. (submitted). The AstraLux

Lucky-imaging data used can be found in Lillo-Box et al. (2024). As highlighted earlier in the paper, only ~ 8 per cent of the host-stars in our sample are lacking imaging observations. Since this is a relatively small number of systems, and they are also homogeneously distributed across different eccentricity ranges (see Fig. 1), this lack of imaging data should not significantly affect our findings. 14 out of the 92 planets in our sample (~ 15 per cent) were found to have a stellar companion detected in the high-resolution imaging data.

To find systems with a wide, co-moving companion, we utilized the El-Badry, Rix & Heintz (2021) catalogue, which made use of *Gaia* eDR3 (Gaia Collaboration 2021) to find spatially resolved binary stars within ~ 1 kpc of the Sun, with projected separations ranging from a few au to 1 pc. 12 out of 92 planets in our sample (~ 13 per cent) belonged to systems containing a wide stellar companion when cross-matched with the El-Badry et al. (2021) catalogue.

The presence of nearby stellar companions has been shown to influence the measured planet parameters (Furlan & Howell 2017) and stellar parameters (Furlan & Howell 2020), in particular with respect to radius. Discovery papers normally take into account the dilution effects on the measured planet and stellar parameters, assuming that the stellar companion was already found at the time of publication. The situation becomes less clear for systems where a nearby stellar companion was only found after the discovery paper was published. To see whether this would pose a problem for companion-detected systems in our sample, we first checked the projected physical separation of the companion candidates, and found that all detected stellar companions (whether found by high-resolution imaging or in the El-Badry catalogue) were relatively distant from the exoplanet host star, with separations larger than 100 au. Additionally, if the companions have angular separations > 5 arcsec, they are usually identified in the *Gaia* data base, and taken into account to estimate the stellar parameters (TIC catalogue) as well as the radius ratio (R_p/R_*) in the transit modelling (TOI catalogue).

Next, for stellar companions with angular separations < 5 arcsec, we checked their magnitude difference ΔM with respect to the host star to see whether they could pose any contamination issues. We found that the majority of the stellar companions detected around our targets are relatively faint ($\Delta M > 5$) and only 3 targets (TOI-2589, TOI-2010 and Kepler-434) had stellar companions that were brighter than $\Delta M = 4$. The discovery papers of TOI-2589 (Brahm et al. 2023) and TOI-2010 (Mann et al. 2023) were aware of the stellar companions and took into account the dilution effect when estimating the stellar and planetary parameters. While the discovery paper of Kepler-434 (Almenara et al. 2015) did not account for the stellar companion, the system was revisited by Berger et al. (2018), who revised Kepler planet radii using *Gaia* DR2, and reported that only low-contrast companions with separations < 4 arcsec could dilute the measured fluxes enough to exceed their reported 8 per cent uncertainties. Given that the companion of Kepler-434 is bound, and its $\Delta M_J = 3$ should correspond to $\Delta M_{K_p} > 4$, it is a relatively high-contrast companion and its dilution effect is almost negligible given the radius uncertainty (as well as uncertainties in stellar parameters).

Fig. 6 shows the eccentricity distribution of planets with no detected stellar companions (blue) versus wide stellar companions (magenta) in our sample. In the no-companion distribution, we excluded planets that had no data available since the presence of companions is uncertain in these cases. If systems lacked imaging observations but were found to have a wide companion, they were not excluded. In summary: systems were only excluded if they lacked high-resolution imaging observations and were also not found in the

⁴<https://exofop.ipac.caltech.edu>

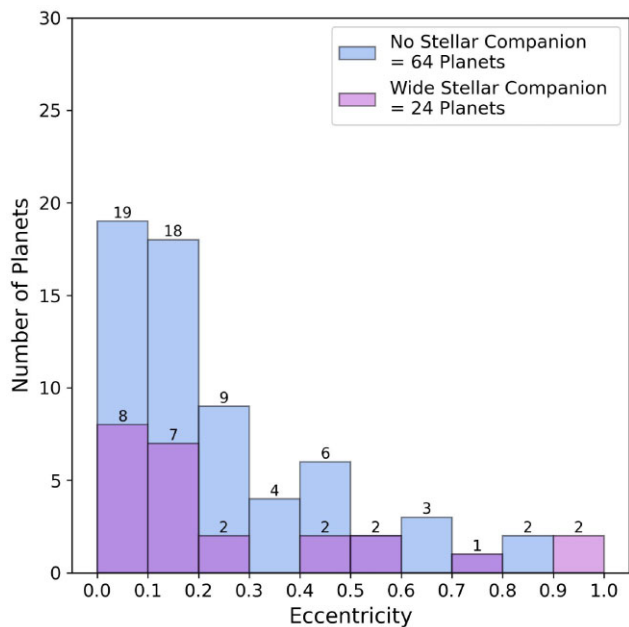


Figure 6. Eccentricity distribution of planets with no detected stellar companions (blue) versus planets with wide stellar companions (magenta) in our sample. 4 out of the 92 planets (~ 4 per cent) were excluded from this sample due to lack of imaging data.

El-Badry et al. (2021) catalogue. This resulted in a total of 4 out of the 92 planets (~ 4 per cent) being excluded due to lack of data. We find a p -value > 0.05 from the K–S test, which indicates that there is no statistical correlation between the planet eccentricity and the presence of stellar companions for TLGs. This could provide important clues about the eccentricity origin for our sample.

Previous studies of eccentricity distributions of small planets and close-in giant planets similarly found no statistical trend with stellar companions. Van Eylen et al. (2019) reported that there was no noticeable difference in the eccentricity distributions of small planets around single stars and those orbiting a star with a close stellar companion. Knutson et al. (2014) also found no eccentricity dependence of close-in giant planets on the presence of stellar companions, as well as no observed difference in the frequency of companions for planets with well-aligned circular orbits and misaligned eccentric orbits. The lack of correlation between the planet eccentricity and the presence of wide stellar companions in our sample indicates that these warm, long-period giant planets may have experienced secular planet–planet scattering, and that the Kozai–Lidov mechanism does not play a critical role in the eccentricity distribution of TLGs.

If more than one giant planet is initially formed in the system, then planet–planet interaction could eject one giant planet out of the system while leaving behind an eccentric giant planet within the system (Lin & Ida 1997). Additionally, Dawson & Murray-Clay (2013) showed strong evidence that gas giants with higher eccentricities (in particular ones orbiting higher metallicity host-stars) are driven by the presence of another giant planet. This is supported by previous works that investigated whether the highly eccentric exoplanet population can be produced entirely by scattering (Ford & Rasio 2008; Carrera, Raymond & Davies 2019). Carrera et al. (2019) showed that the eccentricity distribution for giant planets with $e > 0.3$ was found to be consistent with the planet–planet scattering scenario, and they highlight how the Kozai–Lidov

mechanism is not necessarily the default source of the eccentricity origin for planets discovered with very high eccentricities.

As a sanity check, we roughly estimated the Kozai–Lidov oscillation time-scale for systems with confirmed stellar companions (see Holman, Touma & Tremaine 1997; Shevchenko 2020), and found that for a majority of the targets (>60 per cent), the time-scale is longer than the inferred age of the system, which may be partly responsible for the absence of a correlation between eccentricity and the presence of a stellar companion. It is worth noting though that Kozai–Lidov is predicted to produce planets with high eccentricities and low mutual inclinations, or low eccentricities and high mutual inclinations (Hatzes 2016). In such cases, it could still be possible for the TLGs in our sample to have acquired their eccentricities via the Kozai–Lidov effect. Bowler et al. (2020) used hierarchical Bayesian modelling to test for population-level trends in the stellar companion eccentricity distributions of 27 long-period giant planets and brown dwarfs, where they found significant differences when looking at companion mass and mass ratio. They reported that the stellar companions of giant planets have a preference for low eccentricities ($e \sim 0.05$ – 0.25), which provides evidence for *in situ* formation on largely undisturbed orbits within massive extended disks. If the Kozai–Lidov mechanism is the source of the eccentricity origin for such planets in our sample, we might expect these companions to have lower eccentricities. Further follow-up studies of the mutual inclinations of planets in our sample could help shed light on the prominence of Kozai–Lidov and whether it does indeed play any role, but this is beyond the scope of this paper.

6.3 Planet radius

We explore the dependence of the eccentricity distribution of TLGs on the planet radius R_p . There is an interesting gap in the radius distribution at $\sim 6 R_{\oplus}$ (see Fig. 1), indicating the possibility of two separate populations within our sample. This is further supported by the results of our internal structure modeling (see Section 4), where planets with $R_p > 6 R_{\oplus}$ were found to be gas giants and compositionally different from the smaller planet counterparts below $6 R_{\oplus}$. To test the significance of this using the K–S test, we split our sample based on the planet radius, using a cut-off threshold of $R_p = 6 R_{\oplus}$. Fig. 7 shows the eccentricity distribution of large (blue) versus small (magenta) planets in our sample. Both results from the K–S test and the Spearman ρ test have p -values < 0.05 , indicating that there is a statistical correlation between R_p and eccentricity for TLGs. We can see that the majority of small planets have lower eccentricities, and planets with higher eccentricities tend to be larger.

We found that planet radius plays a significant role in the eccentricity distribution of TLGs, where small versus large planet systems produced statistically different distributions (see Fig. 7), indicating that these two populations are separate and could have different sources for their eccentricity origin. Eccentricity distributions of small planets similarly found a radius correlation. Kane et al. (2012) reported a radius-dependence for *Kepler* candidates, where smaller planets were found to have lower eccentricities. It is important to note that having a mixture of planet groups in our sample (see our internal composition modelling in Section 4) introduces issues such as the planet composition degeneracy for sub-Neptunes, where it is very difficult to differentiate between a rocky core with a gaseous envelope versus a planet with a significant water mass fraction in its atmosphere (water worlds). The formation pathways and eccentricity evolution also vary across different planet groups and will not be the same for all planets in our sample. This highlights the benefit of

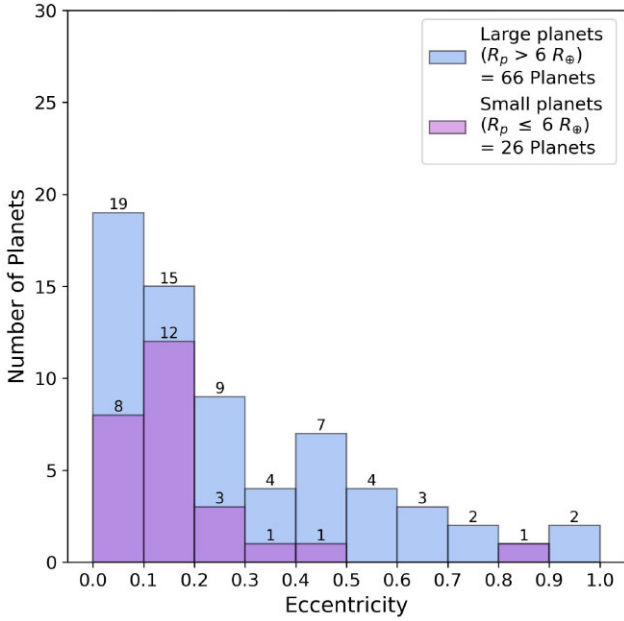


Figure 7. Eccentricity distribution of large (blue) versus small (magenta) planets, using a cut-off threshold of $R_p = 6 R_{\oplus}$.

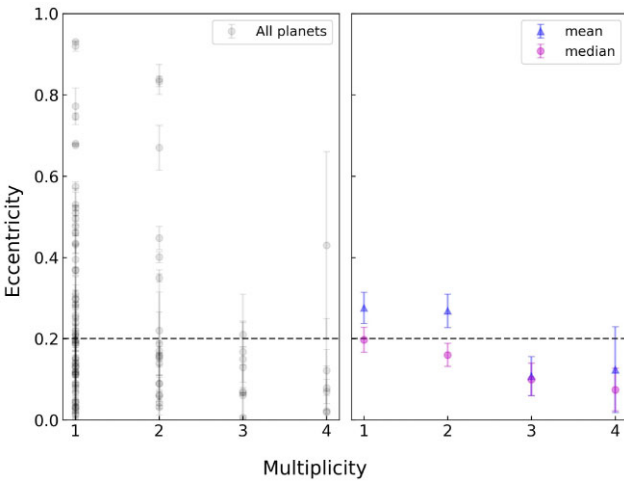


Figure 8. Planet Multiplicity versus Eccentricity for targets in our sample. The left panel shows all the planets in our sample, while the right panel shows the weighted mean and median eccentricity values for each multiplicity bin.

placing more strict radius cuts for future studies in order to separate planet groups with different internal compositions.

6.4 Planet multiplicity

We explore the relation of planet multiplicity N with eccentricity e in our sample of TLGs. Fig. 8 shows the planet multiplicity versus eccentricity for targets in our sample. The largest eccentricities appear to be dominated by single-planet ($N = 1$) and 2-planet ($N = 2$) systems, after which the planet eccentricities quickly fall closer to $e \leq 0.2$ for $N > 2$.

Previous empirical studies have shown an anticorrelation trend between N and e , usually described by a power law in the form of $e(N) = \alpha \times N^\beta$ (Limbach & Turner 2015; Zinzi & Turrini 2017; Bach-Møller & Jørgensen 2021). It is worth noting the different

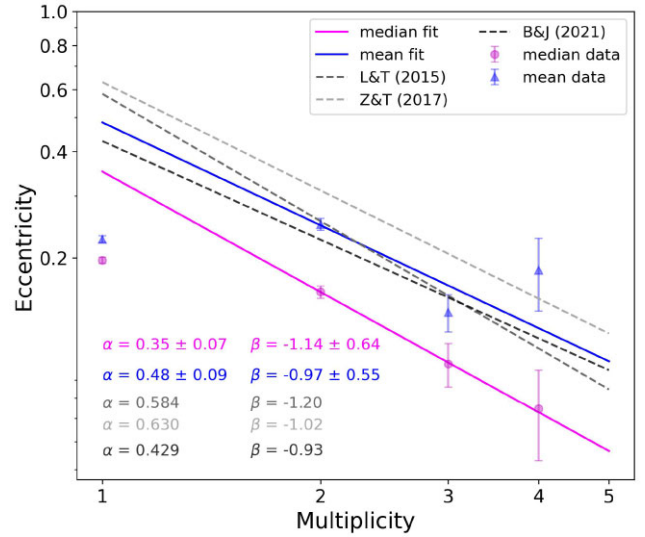


Figure 9. Planet Multiplicity versus Eccentricity for targets in our sample. The solid lines are the best-fitting power-law models to the weighted mean (blue) and median (magenta) eccentricities of our sample (for $N > 1$). For comparison, we also over-plot the power-law trends from Limbach & Turner (2015) (grey), Zinzi & Turrini (2017) (light-grey), and Bach-Møller & Jørgensen (2021) (black) using dashed lines.

selection criteria adopted by these studies. Limbach & Turner (2015) focused on catalogued radial velocity (RV) systems for their sample. Zinzi & Turrini (2017) limited their sample to planets that were around stars with effective temperatures between 2600 and 7920 K, in systems with at least two planets, and were discovered with either the RV or transit methods. Bach-Møller & Jørgensen (2021) did a larger-scale study and included all confirmed planets listed on NEXA, regardless of detection method. The only requirement they placed was for the eccentricity to have error measurements listed on NEXA. As part of their study, they also split their sample into subsets to explore possible correlations (e.g. with planet types and/or detection methods), and found that all sub-samples consistently followed the same basic trend. Our choice to only focus on TLG planets makes our sample distinct in comparison to previous works, all of whom placed no criteria on planet types.

Fig. 9 shows the planet multiplicity N versus eccentricity e for targets in our sample, along with our best-fitting power law models to the weighted mean and the median eccentricities. We also overplot the power-law trends from previous studies to compare with our best-fitting models. Our best-fitting power law to the weighted mean and the median eccentricities is found to be $e(N) = 0.35 \times N^{-1.14}$ and $e(N) = 0.48 \times N^{-0.97}$, respectively.

Finally, we compare the eccentricity distributions for single ($N = 1$) versus multiple planet ($N > 1$) systems (see Fig. 10). We find a p -value < 0.05 from the K-S test, indicating that these two sub-samples of exoplanets are statistically different from each other, and that they could be driven by different evolution paths and processes.

We found that planet multiplicity plays a significant role in the eccentricity distribution of TLGs, where single versus multiplanet systems produced statistically different distributions (see Fig. 10), indicating that these populations could be driven by different evolution paths and processes. The majority of planets with $e > 0.4$ are single-planet systems, while multiplanet systems tend preferentially towards lower eccentricities. These findings are compatible with previous predictions, where high eccentricity planets are more likely

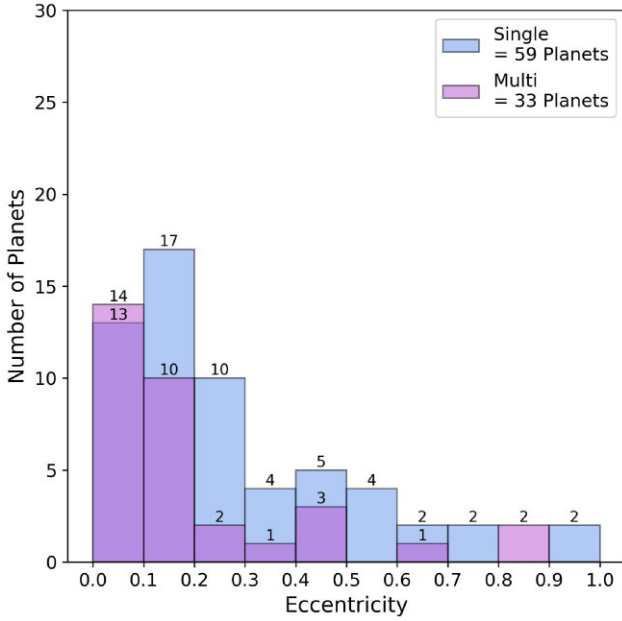


Figure 10. Eccentricity distribution of single (blue) versus multiple (magenta) planet systems in our sample.

to be single planets and multiplanet systems are expected produce lower eccentricities (Kane et al. 2012; Xie et al. 2016). Finally, it is worth noting that single-planet and 2-planet systems are more likely to have longer period companions that have not yet been discovered due to observation or detection limits, so this could also play a role in the inferred correlation between planet multiplicity and eccentricity. Thus, we stress the importance of longer RV follow-up campaigns for the single systems in our sample, where outer planets could still be missing. Another possibility for single-systems with no detected planetary companions could be that the companion could have already been ejected from the system, but there is no way to test or trace this scenario observationally.

The anticorrelation of planet multiplicity and eccentricity has been predicted by past works, where the eccentricity origin of exoplanets is assumed to be predominantly caused by planet–planet interactions (Davies et al. 2014), and was empirically tested in subsequent studies using large samples of RV-detected exoplanets. It is important to note that our sample size (92 planets) is much smaller compared to other studies of planet multiplicity due to our focus on TLGs. While the results may not be statistically significant due to the small sample size, it can be useful to compare them with previous works and see whether we find similar correlations. Limbach & Turner (2015) found a power-law trend of $e(N) = 0.58 \times N^{-1.2}$ for $N > 2$ (using the median eccentricities) for a sample of 403 RV-detected exoplanets with non-zero eccentricities. Zinzi & Turrini (2017) found a power-law trend of $e(N) = 0.63 \times N^{-1.02}$ for $N > 1$ (using the weighted average eccentricities) for a sample of 258 planets around stars with $T_{\text{eff},\star}$ between 2600 and 7920 K. Bach-Møller & Jørgensen (2021) found a power-law trend of $e(N) = 0.43 \times N^{-0.93}$ for $N > 1$ (using the mean eccentricities) for a sample of 1171 exoplanets, the largest statistical sample explored so far. We note that our α value (0.35) is close to the one found by Bach-Møller & Jørgensen (2021), while our β value (−1.13) falls exactly in between what is found by Zinzi & Turrini (2017) and Limbach & Turner (2015). Additionally, we find a similar pattern to Bach-Møller & Jørgensen (2021), where the observed $N = 1$ systems (single-planets) have mean and median

eccentricities much lower than what is expected from the best-fitting models. Bach-Møller & Jørgensen (2021) concluded as a result of this that the single-planet sub-sample is likely affected by different evolutionary pathways in comparison with their multiplanet counterparts, and this might also be the case for the TLGs in our sample. Similar to these previous studies, we found an anticorrelation trend between planet multiplicity and eccentricity for our sample of TLGs, further supporting the conclusion that the eccentricity origin of our targets is most likely dominated by planet–planet interactions.

6.5 Planet equilibrium temperature

We test the dependence of the eccentricity distribution of TLGs on the equilibrium temperature of the planet T_{eq} . We calculate T_{eq} (assuming a Bond albedo of 0) using equation (3) from Kempton et al. (2018), as follows:

$$T_{\text{eq}} = T_{\text{eff},\star} \sqrt{\frac{R_{\star}}{a}} \left(\frac{1}{4}\right)^{1/4} \quad (1)$$

where $T_{\text{eff},\star}$ is the effective temperature of the host star, R_{\star} is the stellar radius, and a is the semi-major axis of the planet. When calculating T_{eq} , we use the JAXSTAR-derived $T_{\text{eff},\star}$ and R_{\star} values for each system. For homogeneity, we use Kepler’s Third Law to calculate a , as follows:

$$a \propto (M_{\star} P^2)^{1/3} \quad (2)$$

where M_{\star} is the JAXSTAR-derived stellar mass and P is the orbital period of the planet.

To check for statistical trends using the K–S test, we split our sample based on whether planets had a cold or hot equilibrium temperature, using $T_{\text{eq}} = 500$ K as the cut-off threshold between the two sub-samples. We adopted this threshold because planets with $T_{\text{eq}} \leq 500$ K were categorized as long-period cold ice/gas giants by previous studies (Konatham, Martin-Torres & Zorzano 2020; Russell 2023), while planets with $T_{\text{eq}} > 500$ K were found to be close-in planets and hot Jupiters (Konatham et al. 2020). Fig. 11 shows the eccentricity distribution of planet systems with hot (blue) versus cold (magenta) equilibrium temperatures in our sample. Both results from the K–S test and the Spearman ρ test have p -values > 0.05 , indicating that there is no statistical correlation between T_{eq} and eccentricity for TLGs. As a sanity check, we tested whether there was any eccentricity correlation with the effective stellar temperature $T_{\text{eff},\star}$. As before, the p -values are larger than 0.05 from both the K–S test and the Spearman ρ test, indicating that there is no statistical correlation between $T_{\text{eff},\star}$ and eccentricity.

While previous statistical studies of eccentricity distributions did not directly test the dependence of eccentricity on the planet equilibrium temperature, other independent studies exploring the habitability of exoplanets have looked into this extensively. Dressing et al. (2010) showed that planets with higher eccentricities could remain habitable at much larger semi-major axes. They also reported that larger eccentricities caused planet temperatures to experience increased regional and seasonal variability, leading to a more gradual transition between habitable and non-habitable zones. Another study by Linsenmeier, Pascale & Lucarini (2015) reported that eccentric orbits typically resulted in two stable climate states, although the range was more limited. Perhaps the most relevant dependence found with respect to our study was reported by Méndez & Rivera-Valentín (2017), who found that for a constant albedo, a planet’s average equilibrium temperature is expected to

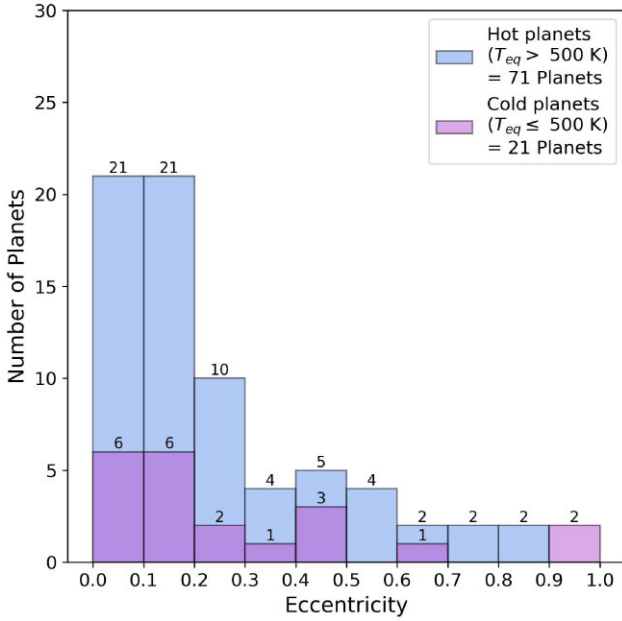


Figure 11. Eccentricity distribution of systems with hot (blue) versus cold (magenta) planet equilibrium temperatures in our sample, using 500 K as the cut-off threshold between the two sub-samples.

decrease as the eccentricity increases. We found no such correlation in our sample of TLGs, but this trend could yet be verified by extending the sample size to include non-transiting, long-period giant planets.

6.6 Tidal dissipation

We explore the relationship between the eccentricity distribution of TLGs and the tidal dissipation effects on the planet.

6.6.1 Circularization time-scale

We calculate the tidal circularization time-scale t_{circ} using equation (1) from Trilling (2000) or equation (4) from Jackson, Greenberg & Barnes (2008), as follows,:

$$t_{\text{circ}} = Q_p \sqrt{\frac{a}{GM_\star}} \left(\frac{4}{63}\right) \left(\frac{M_p}{R_p^5}\right) a^6 \quad (3)$$

where Q_p is the modified tidal quality factor of the planet, a is the orbital semi-major axis of the planet, G is the gravitational constant, M_\star is the stellar mass, M_p is the planet mass, and R_p is the planet radius. Q_p encompasses the proper quality factor Q , as well as the planet Love number k_2 , given by $Q_p = (3/2) \times (Q/k_2)$. While equation (3) is not strictly appropriate for higher eccentricity regimes (e.g. $e \geq 0.2$), it can be suitable to use when trying to estimate the current eccentricity damping time-scale. The large uncertainties in the constant time lag approach and the constant tidal quality factor approach, coupled with our ignorance about the initial conditions of the system, make a detailed computation of the evolution of the eccentricity very difficult. In such cases, equation (3) can provide a good estimate of the present-day eccentricity damping time-scale. In general, the energy change of a planet due to strong tidal interactions with the host star can be estimated as an impulse approximation, which is strongly dependent on the pericentric distance q . When q is large enough (e.g. $q > 0.05$ – 0.1 au), the tidal interactions are too

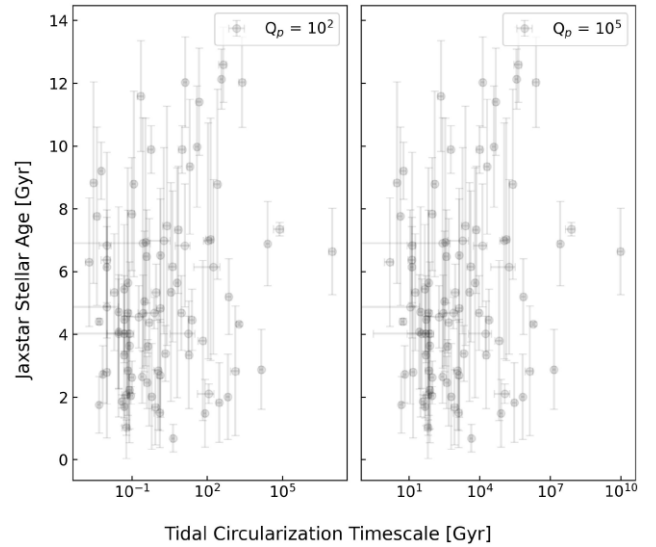


Figure 12. Tidal circularization time-scale versus stellar age t_{age} for targets in our sample, assuming constant Q_p scale factors of 10^2 (left) and 10^5 (right) for all planets in our sample.

inefficient to damp the planet’s eccentricity and semi-major axis. In such cases, the time-scale ratio τ (the ratio between the stellar age and the planet tidal circularization time-scale; see Section 6.6.4) of high- e planets must be small, as shown in Figs 16 and 17 as well.

When calculating t_{circ} , we use the JAXSTAR-derived stellar mass for M_\star (see Section 3 for more details). a is calculated using Kepler’s Third Law, as shown in equation (2). Finally, we tested two different Q_p cases when calculating t_{circ} : a constant Q_p value and a varying Q_p value (see Section 6.6.2 for more details).

6.6.2 Tidal quality factor

We tested two different Q_p cases when calculating the tidal circularization time-scale t_{circ} : a constant Q_p value and a varying Q_p value. For the constant Q_p scale factor, we tested 4 different values across the entire target list: 10^2 , 10^3 , 10^4 , and 10^5 . Fig. 12 shows the tidal circularization time-scale t_{circ} versus stellar age t_{age} for all planets in our sample, assuming constant Q_p scale factors for all planets in our sample.

The rheological response and viscosity of planetary materials contribute to the efficiency of tidal dissipation. The tidal quality factor should be related to the internal composition and the thermal state of a planet. To determine how to appropriately estimate varying Q_p values for our target list, we use the results of our internal composition modeling, as described in Section 4. If the interior of a planet can have a significant H/He envelope, we adopt high Q_p values for gas giants. For bare rocky planets or rocky planets with < a few % H/He envelopes, we use low Q_p values similar to those for terrestrial planets. A planet that may contain a water mantle is assumed to have intermediate Q_p values, such as Uranus and Neptune. Following the concept above, planets in groups (i) and (ii) are expected to have high Q_p values ($\sim 10^4$ – 10^5), while planets in groups (iii) and (iv) are expected to have intermediate Q_p values ($\sim 10^2$ – 10^3), and group (v) planets are expected to have low Q_p values (~ 10 – 100). Based on this, we divided our sample into 3 categories depending on their radius, and we assigned different Q_p values to the planets in each category as follows:

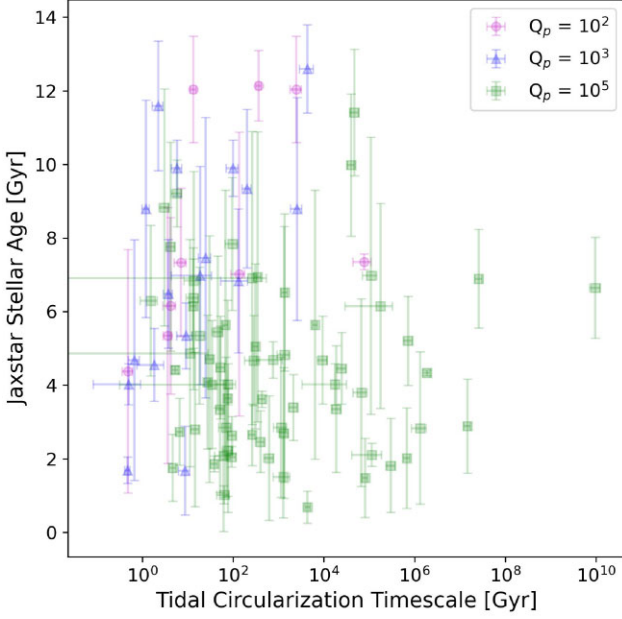


Figure 13. Tidal circularization time-scale versus stellar age t_{age} for targets in our sample, assuming varying Q_p scale factors based on the planet’s radius. We highlight the Q_p values of 10^2 , 10^3 , and 10^5 in circle points, triangle points and square points, respectively.

- (i) High Q_p (10^5): planets with $R_p > 6 R_{\oplus}$
- (ii) Intermediate Q_p (10^3): planets with $3 R_{\oplus} < R_p < 6 R_{\oplus}$
- (iii) Low Q_p (10^2): planets with $R_p < 3 R_{\oplus}$

Fig. 13 shows t_{circ} versus t_{age} again, but assuming varying Q_p scale factors for the planets in our sample using the parametrization based on the planet’s radius.

6.6.3 Short versus long tidal time-scale planets

To compare the eccentricity distribution of planets with short versus long tidal circularization time-scales, we define the time-scale ratio τ (the ratio between the stellar age t_{age} and the planet’s tidal circularization time-scale t_{circ}) as follows:

$$\tau = \frac{t_{\text{age}}}{t_{\text{circ}}} \quad (4)$$

For t_{age} , we use the JAXSTAR-derived stellar ages, as described in Section 3. We use the time-scale ratio to split our sample using a cut-off threshold of $\tau = 0.9$ when checking for statistical correlations using the K–S test. At $\tau = 1$, t_{circ} is as long as the age of the system t_{age} . Since t_{circ} is still very close to the age of the system at $\tau = 0.9$, we chose to use 0.9 as the cut-off instead of 1. When $\tau > 0.9$, t_{age} is longer than t_{circ} , meaning that the planet is likely to circularize during its lifetime. When $\tau \leq 0.9$, t_{circ} is longer than t_{age} , indicating that the planet is not likely to circularize during its lifetime and will retain its present eccentricity.

We computed the eccentricity distribution of planets with long (blue) versus short (magenta) tidal circularization time-scales with respect to their host-star age (using a cut-off of $\tau = 0.9$), assuming 4 constant Q_p scale factors (10^2 , 10^3 , 10^4 , and 10^5). We performed statistical tests to check the significance of the two distributions for each constant Q_p value. Both results from the K–S test and the Spearman ρ test have p -values > 0.05 for Q_p scale factors of 10^3 , 10^4 , and 10^5 , indicating that there is no statistical significance

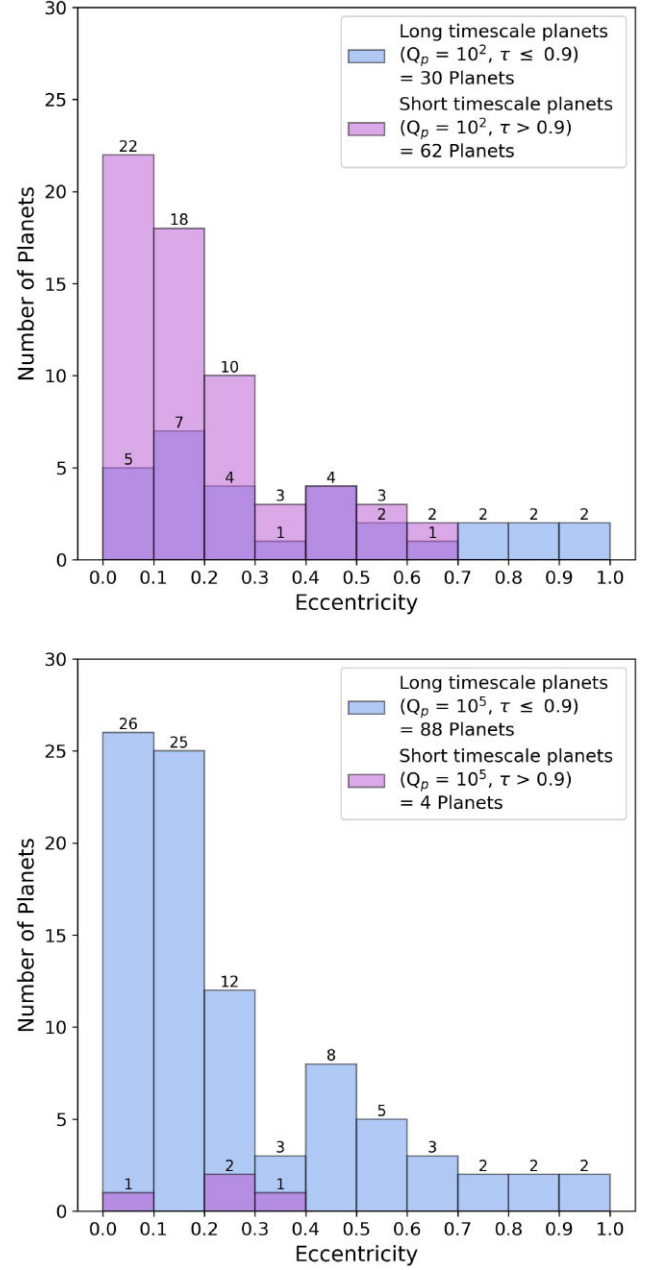


Figure 14. Eccentricity distribution of planets with long (blue) versus short (magenta) tidal circularization time-scales with respect to their host-star age (using a cut-off of $\tau = 0.9$), assuming constant Q_p scale factors of 10^2 (top) and 10^5 (bottom).

between the short versus long time-scale distributions for these cases. For the for $Q_p = 10^2$ case, the K–S test has a p -value < 0.05 , while the Spearman ρ test yields a p -value > 0.05 . Fig. 14 shows the eccentricity distributions for the lowest (10^2) and highest (10^5) Q_p scale factor values.

Fig. 15 shows the eccentricity distribution of planets with long (blue) versus short (magenta) tidal circularization time-scales with respect to their host-star age (using a threshold of $\tau = 0.9$) assuming 3 varying Q_p scale factors based on the planet composition. We performed K–S tests to check the significance of the two distributions, and find a p -value of 0.31 ($p > 0.05$), indicating that there is no

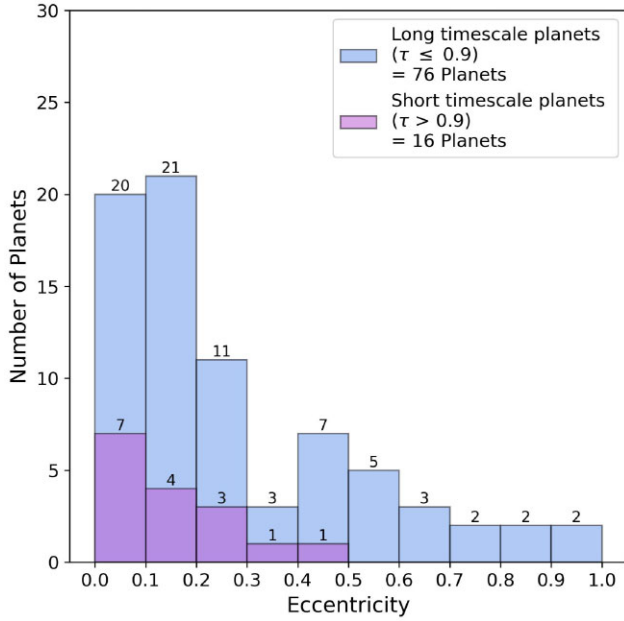


Figure 15. Eccentricity distribution of planets with long (blue) versus short (magenta) tidal circularization time-scales with respect to their host-star age (using a cut-off threshold of $\tau = 0.9$) assuming varying Q_p scale factors based on the planet composition.

statistical significance between the short versus long time-scale distributions.

6.6.4 Time-scale ratio

Since we can only broadly estimate what the appropriate Q_p values are for our TLG sample, we choose to focus on the general trend observed in the time-scale ratio τ with respect to eccentricity, so that our findings will not be dependent on which Q_p values are assumed.

Fig. 16 shows the time-scale ratio τ versus eccentricity e for targets in our sample, assuming constant Q_p scale factors, while Fig. 17 shows the same plot but for varying Q_p scale factors. We find a ‘forbidden’ zone, marked by the grey shaded areas in the plots.

In the constant Q_p case, we find that there are no planets with eccentricities of $e \geq 0.4$ beyond a given τ , regardless of the Q_p scale factor used. In the varying Q_p case, we highlight 2 different ‘forbidden’ zones. The first zone is marked by dark-grey shaded region in the plot, where there are no planets with eccentricities of $e > 0.6$ beyond a given τ . The second zone is marked by the light-grey shaded region after excluding one target, Kepler-89 c (TIC 273231214), which has large uncertainties on its eccentricity measurement. When excluding Kepler-89 c, this second ‘forbidden’ zone extends down to $e \sim 0.1$, beyond which there are no planets.

6.6.5 Implications

There is still much work to be done when it comes to understanding how best to quantify Q_p based on planet properties (e.g. density, equilibrium temperature, etc.) (Mathis 2018). Some studies have tried to estimate Q_p using tidal dissipation measurements of Solar System planets and moons (Lainey et al. 2009; Fuller et al. 2024), which could in theory help us apply them to exoplanets (Dhouib et al. 2023; Lazovik et al. 2024). Giant planets are more likely to have higher Q_p values (e.g. 10^4 – 10^5) (Mahmud, Penev & Schussler

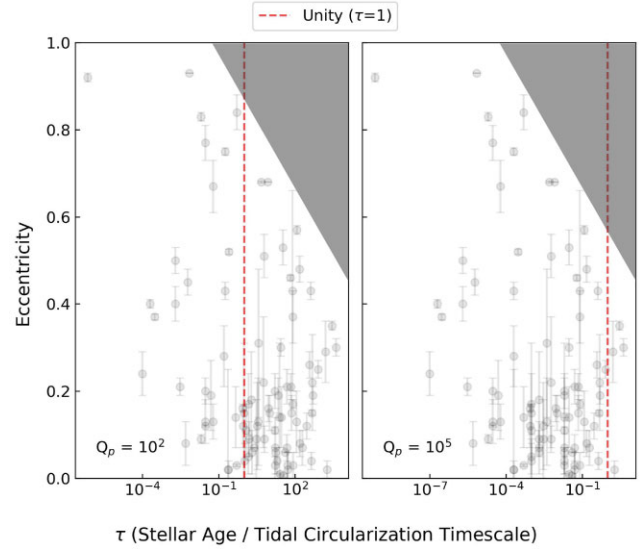


Figure 16. Time-scale ratio τ versus eccentricity e for targets in our sample, assuming constant Q_p scale factors. For reference, we also show the unity of τ , where $t_{\text{age}} = t_{\text{circ}}$, using a vertical dashed line. The shaded areas mark the ‘forbidden’ zone, where planets at higher eccentricities are not found beyond a given τ .

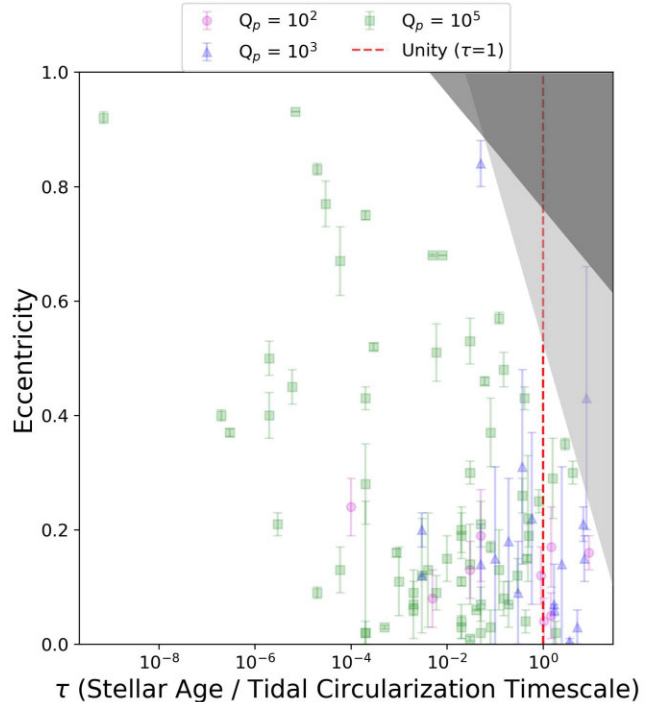


Figure 17. Time-scale ratio τ versus eccentricity e for targets in our sample, assuming varying Q_p scale factors. For reference, we also show the unity of τ , where $t_{\text{age}} = t_{\text{circ}}$, using a vertical dashed line. The dark shaded region marks the ‘forbidden’ zone, where planets at higher eccentricities are not found beyond a given τ . The light shaded region shows the ‘forbidden’ zone after excluding Kepler-89 c (TIC 273231214), which has large uncertainties on its eccentricity measurement.

2023), but there is still no direct way to map Q_p quantitatively (or with a good degree of certainty) to exoplanets based on their observed properties.

Since we are targeting TLGs in our sample, and Q_p values of $\sim 10^5$ are more likely for Jovian planets, we take a closer look at the $Q_p = 10^5$ for the constant Q_p case in Fig. 16 (the right-most panel). Almost all planets are located to the left of the red-dashed line (the unity of the time-scale ratio τ , where $t_{\text{age}} = t_{\text{circ}}$), meaning that the majority of planets in our sample are not likely to circularize during their lifetime (see the eccentricity distribution in Fig. 14 for the same constant Q_p value, where only 4 planets have expected tidal time-scales shorter than their host-star age).

In the varying Q_p case, our internal composition modelling revealed that the majority of our targets are Jovian planets, where high Q_p values ($\sim 10^5$) are more likely, which is consistent with what is expected for TLGs. In this case as well, Fig. 17 shows that almost all planets are located to the left of the red-dashed line (the unity of the time-scale ratio τ , where $t_{\text{age}} = t_{\text{circ}}$). This indicates that we might be probing the intrinsic, initial state of the system's eccentricity and that the majority of planets in our sample are not likely to circularize during their lifetime (see also the eccentricity distribution in Figs 14 and 15, where only 4 and 16 planets have expected tidal time-scales shorter than their host-star age, respectively).

Our findings from both Q_p cases indicate that the eccentricity distributions of our TLG sample might be a reflection of their primordial state, without having experienced any significant tidal dissipation. The lack of strong tidal dissipation effects further reinforces our finding that the orbital eccentricity of TLGs does not seem to correlate with the presence of stellar companions (as discussed in Section 6.2).

Lastly, we find an interesting ‘forbidden’ zone, marked by the grey shaded areas in Figs 16 (constant Q_p) and 17 (varying Q_p), where planets at higher eccentricities are not found beyond a given τ , regardless of the Q_p scale factor used. The forbidden zone could indicate that the intrinsic eccentricity distribution in our sample is expected to be at τ values much shorter than 1. For instance, in Fig. 17, the intrinsic eccentricity distribution is likely only visible in τ smaller than where the forbidden region is (e.g. less than $\sim 10^{-3}$).

There are several possible scenarios to explain the origin of the forbidden zone. The first scenario could be that planets with high eccentricities are no longer able to form at larger τ values. Without a (sub-)stellar companion or other massive planets in the vicinity, highly eccentric planets would not be able to form in the forbidden region of the system due to the absence of strong perturbers. However, planets may well form with high eccentricity in that region, but they could be subject to a fast eccentricity decay, removing them from the forbidden zone. An alternative scenario could be related to strong tidal interactions between the planet and its host star. Planets with high eccentricities should have experienced strong tidal interactions if their pericentric distance q is small enough (e.g. $q < 0.05$ au) during their closest approach to their host star, after which their eccentricity and semi-major axis decrease rapidly due to small tidal damping time-scales. In the case of tidal interactions, the eccentricity damping time-scale is comparable to the orbital decay time-scale, meaning that planets will have moved closer to their host star in this scenario. Currently, we see that these planets have low eccentricities at small semi-major axes, and planets in the forbidden zone may have disappeared. As a result, we would not expect to see any planets with high eccentricities and large τ values. The habitat of planets in a circular orbit around 0.1 au may originate from tidal circularization of planets in the forbidden region.

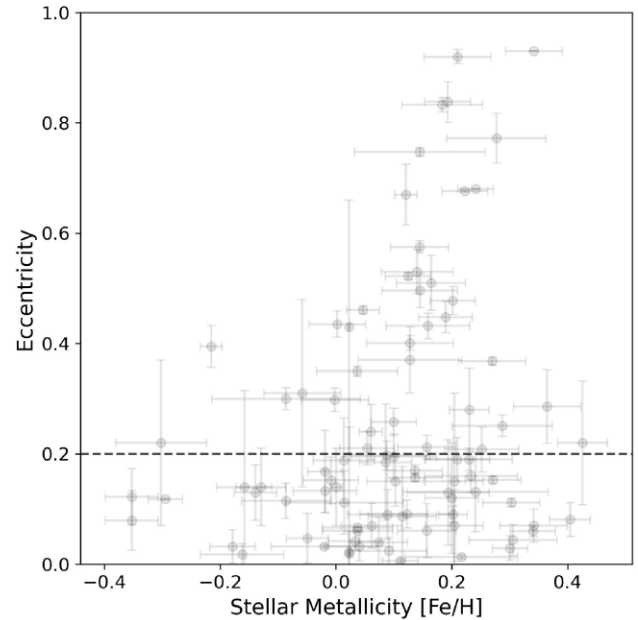


Figure 18. Stellar Metallicity [Fe/H] versus Eccentricity for all 92 planets in our sample.

Interestingly, we found that high- e planets (most of which are gas giants with high Q_p values) tend to have lower τ values, suggesting that the orbits of low- e planets are susceptible to tidal circularization. Udry & Santos (2007) reports that for periods in the range $P \sim 10$ – 30 d, which is considered to be distinctly outside the circularization period by tidal interaction with the star, there are a few systems with very low eccentricities. As part of our sample selection criteria, we placed a period cut of $P > 10$ d to exclude planets that would be severely affected by tides, but the low- e planets in our sample still appear to be sensitive to it.

6.7 Stellar metallicity

We explore the stellar metallicity correlation to the planet eccentricity for our sample of TLGs. Fig. 18 shows the stellar metallicity [Fe/H] versus eccentricity for all 92 targets in our sample. A visible trend can be seen in the data, where host-star metallicities are homogeneously distributed for planets with $e \leq 0.4$, but narrow down significantly at higher eccentricities around $\sim 0.1 < [\text{Fe}/\text{H}] < 0.3$. Fig. 18 clearly indicates that highly eccentric planets are only found around metal-rich stars with $[\text{Fe}/\text{H}] > 0.1$.

To test the statistical significance of this correlation using the K–S test, we split our sample based on whether planets belong to lower or higher metallicity host-stars, using $[\text{Fe}/\text{H}] = 0.1$ as the cut-off threshold between the two sub-samples. This threshold was chosen based on the median metallicity of our sample. We compare the eccentricity distributions of the two sub-samples in Fig. 19. We find that there are no planets beyond $e > 0.4$ in the lower metallicity host-star sample, while the higher metallicity host-star sample includes planets across the entire range of eccentricities. Both results from the K–S test and the Spearman ρ test have p -values < 0.05 , indicating that there is metallicity dependence on eccentricity.

Previous studies show that metal-rich stars have a higher probability of harbouring a giant planet than their lower metallicity counterparts (Udry & Santos 2007), highlighting the crucial role metallicity plays in the formation and evolution of giant planets. In

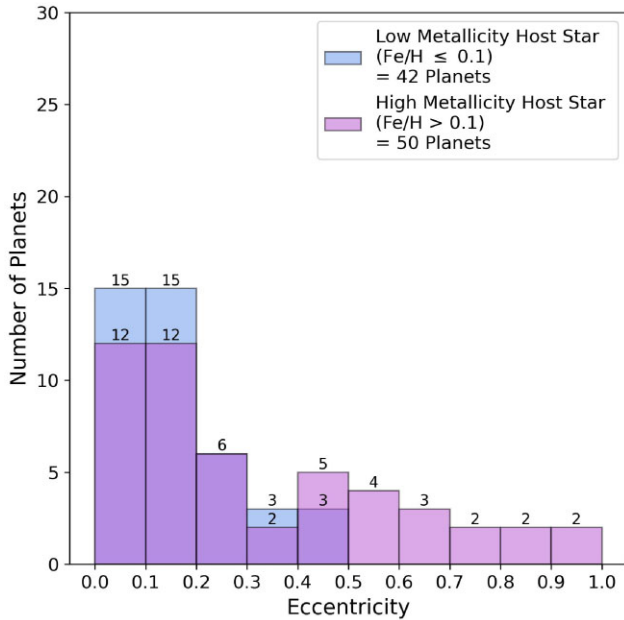


Figure 19. Eccentricity distribution of planet systems with lower (blue) versus higher (magenta) metallicity host-stars in our sample, using $[\text{Fe}/\text{H}] = 0.1$ as the cut-off threshold between the two sub-samples.

fact, many papers have found that stars hosting giant planets were observed to be more metal-rich (Fuhrmann, Pfeiffer & Bernkopf 1997; Gonzalez 1997; Santos, Israelian & Mayor 2001; Fischer & Valenti 2005; Bond et al. 2006). Additionally, the frequency of planets (regardless of eccentricity) is found to be higher around metal-rich host stars, and the dependence of planet abundance on stellar metallicity has been widely known and extensively studied (Bond et al. 2006; Adibekyan 2019). Bond et al. (2006) found that planet-hosting stars were observed to have significantly higher mean metallicities ($[\text{Fe}/\text{H}] = 0.06 \pm 0.03$ dex) compared to non-planet-hosting stars ($[\text{Fe}/\text{H}] = -0.09 \pm 0.01$ dex). Interestingly, Adibekyan (2019) mentions the necessity of separating hot and cold Jupiters when deriving metallicity correlations. This is because the orbital period of giant planets also correlates with metallicity, and longer-period cold giant planets tend to orbit more metal-poor stars than their shorter-period hot giant planet counterparts.

In our study, we found a clear correlation between stellar metallicity on the eccentricity distribution of TLGs, a dependence which was only previously proven for close-in giant planets (Dawson & Murray-Clay 2013). Relations between the stellar metallicity and other planetary orbital parameters have also been previously explored (e.g. e , a , and $M_p \sin i$), but no significant trends have been found (Laws et al. 2003; Santos et al. 2003; Fischer & Valenti 2005). While Santos et al. (2003) reported that there were no statistical correlations between planet eccentricity and the stellar metallicity, their findings suggested that low $[\text{Fe}/\text{H}]$ stars appear to only host planets with intermediate eccentricities, and more eccentric planets were only found around stars with higher metallicities. These findings are in agreement with our results, which show a statistically significant correlation between metallicity and eccentricity. Planets belonging to lower metallicity host-stars ($[\text{Fe}/\text{H}] \leq 0.1$) in our sample only had eccentricities up to $e = 0.4$, indicating that these stars can only host low to moderate eccentricity planets. In contrast, planets belonging to higher metallicity host-stars ($[\text{Fe}/\text{H}] > 0.1$) spanned the entire range of eccentricities ($0 < e < 1$).

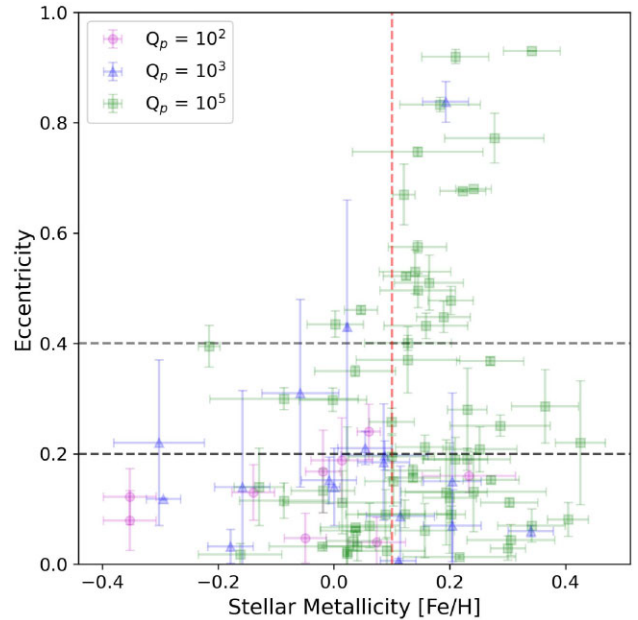


Figure 20. Stellar Metallicity $[\text{Fe}/\text{H}]$ versus Eccentricity for all 92 planets in our sample. The data points are coloured according to the varying Q_p values estimated from the internal composition modeling of the planets. We highlight the Q_p values of 10^2 , 10^3 , and 10^5 in circle points, triangle points and square points, respectively.

A metallicity dependence suggests that more giant planets are expected to form around host-stars with higher $[\text{Fe}/\text{H}]$, with some planets having more enhanced eccentricities and others being entirely ejected from the system. Similarly, since low- $[\text{Fe}/\text{H}]$ stars form fewer large planets, low- $[\text{Fe}/\text{H}]$ stars could be hosting more low- e planets due to the lack of giant planets that could cause eccentricity excitation via planet–planet scattering. For low- e gas giants found around low- $[\text{Fe}/\text{H}]$ stars, planet–planet scattering is unlikely to occur because gas giants form preferentially in metal-rich environments by the core accretion model. Several directly imaged gas giants on wide orbits, which are difficult for the core accretion model to form, have been found around metal-poor stars, such as the multigas giant system around HR 8799. A low $[\text{Fe}/\text{H}]$ could be favourable for the disc instability scenario.

Fig. 20 shows a plot of $[\text{Fe}/\text{H}]$ versus e , coloured according to the varying Q_p values estimated from the internal composition modelling of the planets. For clarity, we display two horizontal grey dashed lines at $e = 0.2$ (below which planets are broadly considered to have low- e or non-eccentric orbits) and $e = 0.4$ (the eccentricity up to which disc migration could occur and be a possible source of the planet’s eccentricity (Bitsch & Kley 2010; Debras, Baruteau & Donati 2021)). The vertical dashed red line at $[\text{Fe}/\text{H}] = 0.1$ is the cut-off threshold used to split our planet sample between lower-metallicity and higher-metallicity host stars. The plot shows that there is a mixture of planet compositions at low $[\text{Fe}/\text{H}]$ (to the left side of the red dashed line), even up to $e = 0.4$. In contrast, gas giants (with the highest Q_p value, coloured in green) appear to dominate more at higher $[\text{Fe}/\text{H}]$ (to the right side of the red dashed line). For the subset of low- e gas giants found at lower metallicities, disc instability could be a more plausible scenario for the origin of these systems.

Additionally, we checked whether there is any visible correlation between planet multiplicity and the presence of low- e planets around low $[\text{Fe}/\text{H}]$ stars. Fig. 21 shows a plot of $[\text{Fe}/\text{H}]$ versus e , coloured

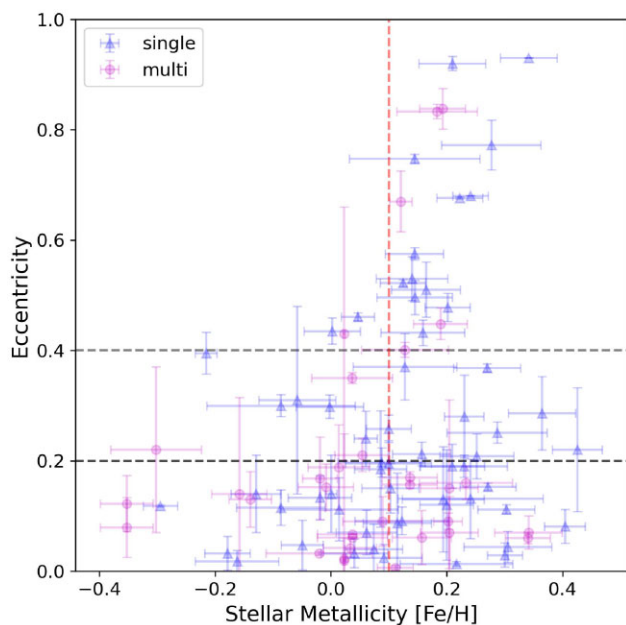


Figure 21. Stellar Metallicity [Fe/H] versus Eccentricity for all 92 planets in our sample. The data points are coloured according to the planet multiplicity, with single systems and multiplanet systems highlighted in blue triangle points and circle magenta points, respectively.

according to planet multiplicity. As before, we display two horizontal grey dashed lines at $e = 0.2$ and $e = 0.4$. We find no visible trend for planet multiplicity within the low- e and low-[Fe/H] planet regime.

Knierim, Shibata & Helled (2022) explored the origin of warm Jupiters within the context of planet formation theory, where the two leading models are (i) formation at the outer disc followed by migration and (ii) *in situ* formation. They found that migrating giant planets had 2–14 times higher metallicities than planets that formed *in situ*, and that the metallicity of migrating planets increased with decreasing planetary mass, but was constant for *in situ* formation. This could mean that disc migration is more favourable for high [Fe/H] giant planets in our sample (up to $e = 0.4$) rather than forming *in situ* and being excited via planet–planet scattering.

7 POSSIBLE BIASES

The statistical study of the eccentricity distribution of long-period giant planets has not been previously well explored. This could in part be due to the ongoing challenges with the detection and characterization of long-period planets, in particular with respect to the long radial velocity (RV) coverage required to accurately characterize such systems and determine their eccentricities (Lagrange et al. 2023). This becomes especially challenging with the presence of stellar and instrumental noise, which are commonly prevalent in RV data and cause contamination depending on the magnitude of the target and the level of its magnetic activity.

It is important to emphasize that the findings of this paper could be biased due to the small sample size, and the target list is not large enough to make any conclusive statements with regards to the wider sample of long-period giant planets. In Section 2, we described the different criteria we used to select our sample, and our decision to focus on transiting systems ultimately limited the sample size. Additionally, we did not place any radius cuts, so our target list includes a mixture of different types of planets with

varying compositions (see the results of our internal composition modeling in Section 4). Interestingly though, Shen & Turner (2008) explored different biases arising from RV surveys in relation to the eccentricity distribution of exoplanets, and found that the detection efficiency only slightly decreased with eccentricity. They reported that the main source of uncertainty in the eccentricity distribution came from biases in Keplerian fits to data with low RV amplitudes and a limited number of observations, rather than from selection effects. Thus, long-baseline RV campaigns would be very useful for sampling the eccentricity distribution of long-period giant planets.

Another potential observational bias is the heterogeneity of the high-resolution imaging data used in this sample. As discussed in Section 6.2, different telescopes and imaging techniques were used, which resulted in different detection limits. Some targets have a combination of imaging observations that are complementary to each other (e.g. AO + Speckle), which make them more reliable when determining the presence of stellar companions. We also mentioned previously how a small number of targets were missing high-resolution imaging altogether, making the sample ~ 8 per cent incomplete. In the ideal case, in order to have a more homogeneous sample of imaging data, all targets would be observed with high-resolution imaging, with multiple complementary observations utilizing both AO and Speckle techniques, and preferably observed with the same telescopes.

We would also like to highlight that this might not be the ideal target list for this type of study, and follow-up analyses that expand this target list to a larger sample (e.g. including non-transiting systems), or place a more rigorous focus on planet composition (e.g. by introducing strict radius cuts) would be beneficial for future work on the eccentricity origin of long-period giant planets. Performing a homogeneous re-fitting of the radial velocity data would also be ideal in order to counter any possible biases introduced in the reported planet properties as a result of heterogeneous analyses, but this is beyond the scope of this paper. Large RV campaigns dedicated to monitoring long-period giant planets could play a key role in the eccentricity distributions of these planets, which have otherwise not been well explored. Other approaches suggest utilizing hierarchical Bayesian modeling to infer the true eccentricity distribution rather than using a histogram of estimated eccentricities, which could be beneficial for future large-scale population studies (Hogg, Myers & Bovy 2010).

Finally, while we found correlations for stellar metallicity, planet radius and planet multiplicity with the planet eccentricity, there is a possibility that these parameters are correlated with each other, and this could be contributing to their individual correlations with the planet’s eccentricity. In other words, there could be correlations between these parameters that are independent of eccentricity. To test whether this is the case, we performed K–S tests between these three parameters. We found a strong dependence of planet radius on planet multiplicity (p -value = 0.0002), and planet radius on stellar metallicity (p -value = 0.0007), while no correlations were found between planet multiplicity and stellar metallicity (p -value = 0.12). Fig. 22 shows the radius distribution for single versus multiplanet systems. Interestingly, we can see a bimodal radius distribution for single-planet systems, with a gap between $R_p = 6\text{--}7 R_{\oplus}$. Additionally, the majority of these planets appear to be clustered towards larger radii ($R_p > 7 R_{\oplus}$). In contrast, the multiplanet systems show a more flat radius distribution, with no gap separating small versus large planets. This suggests that single-systems could be more sensitive to formation processes that produce smaller planets compared to their larger counterparts. However, we highlight that this could also be a result of observational bias since larger planets

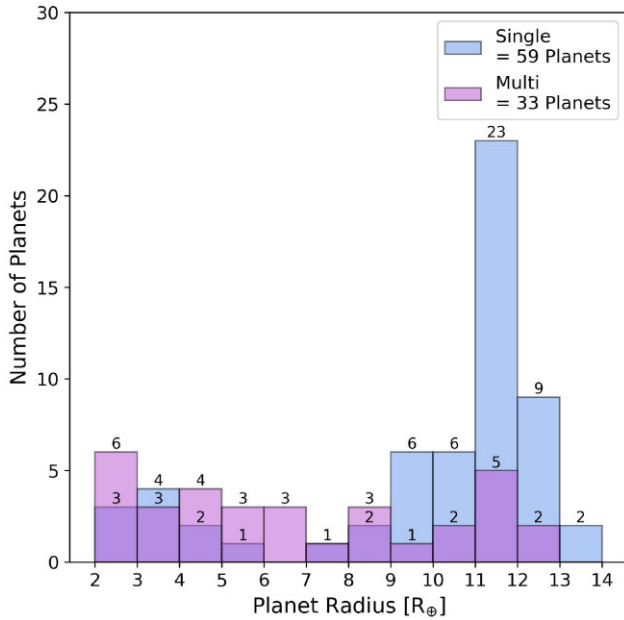


Figure 22. Radius distribution of single (blue) versus multiple (magenta) planet systems in our sample.

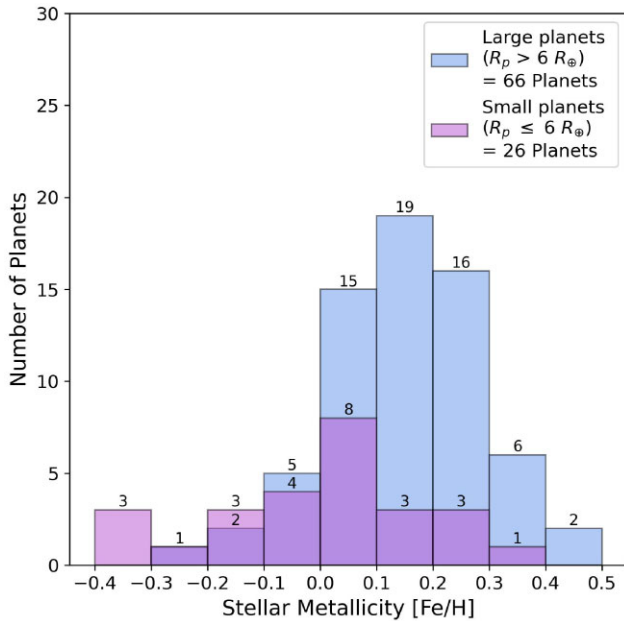


Figure 23. Stellar Metallicity distribution of large (blue) versus small (magenta) planets, using a cut-off threshold of $R_p = 6 R_{\oplus}$.

are easier to detect, coupled with the fact that many single-systems might not be followed up with studies that would detect possible outer companions if any exist. For eccentricity distributions of small planets ($R_p = 1\text{--}6 R_{\oplus}$), Van Eylen et al. (2019) found that the planet radius did not play any significant role for single versus multiplanet systems, indicating that multiplicity does not depend on the planet size when the small versus large planet populations are separated. Fig. 23 shows the stellar metallicity distribution as a function of planet radius. Larger planets ($R_p > 6 R_{\oplus}$) are found to be more abundant at higher metallicities, which is consistent with theoretical predictions since giant planets are expected to form more around metal-rich stars. Since stellar metallicity and planet multiplicity

were not found to be correlated with each other, they are likely independently correlated with eccentricity. However, we found a strong radius correlation with other parameters, since both metallicity and multiplicity were sensitive to the planet size. As a result, the inter-dependencies between radius and these other parameters could partially be responsible for its mutual correlation with the eccentricity distributions of TLGs.

8 SUMMARY AND CONCLUSIONS

Eccentric giant planets are predicted to have acquired their eccentricity through two major mechanisms: the Kozai–Lidov effect or planet–planet scattering, but it is usually difficult to distinguish between the two mechanisms and determine the true eccentricity origin for a given system. A population study on a statistical level for the observed distribution of such planets could provide better insights into their eccentricity origins and evolution history. In this work, we focus on a sample of 92 transiting, long-period giant planets (TLGs) as part of an eccentricity distribution study for this planet population in order to understand their eccentricity origin. We used archival high-contrast imaging observations, public stellar catalogues, precise *Gaia* astrometry, and the NASA Exoplanet Archive database, to explore the eccentricity distribution correlation with different planet and host-star properties, including: stellar age, stellar companion, planet radius, planet multiplicity, planet equilibrium temperature, planet tidal dissipation time-scale, and stellar metallicity. To mitigate biases in heterogeneous model fits, we homogeneously characterized the basic stellar properties for all 86 host-stars in our sample, including stellar age and metallicity.

We found that the planet eccentricity of TLGs depends on stellar metallicity, planet radius, and planet multiplicity. Our findings show that lower-metallicity stars ($[\text{Fe}/\text{H}] \leq 0.1$) did not host any planets beyond $e > 0.4$, while higher-metallicity stars hosted planets across the entire eccentricity range ($0 < e < 1$). Additionally, planet multiplicity played a significant role in the eccentricity distribution of TLGs, where the majority of planets with $e > 0.4$ were single-planet systems, while multiplanet systems leaned preferentially towards lower eccentricities. The correlation found for planet radius showed that separate planet populations exist within our sample. This was further supported by the results of our internal composition modeling, which revealed a mixture of planet groups.

We also explored the general trend observed in the time-scale ratio τ with respect to eccentricity, so that our findings were not dependent on which Q_p values were assumed when determining the tidal circularization time-scales of our planets. We found an interesting ‘forbidden’ zone, where there were no planets with high eccentricities and large τ values. There are several possibilities for the origin of this zone: (1) planets at higher eccentricities are no longer able to form beyond a given τ , (2) planets form with high eccentricity but are removed from the forbidden zone after experiencing a fast eccentricity decay, or (3) the eccentricities of these planets decrease rapidly due to strong tidal interactions at large τ values. The general trend indicates that the eccentricity distributions of our TLG sample might be a reflection of their primordial state, with a lack of strong tidal dissipation effects. Interestingly, we found no correlation between the eccentricity distribution and the presence of stellar companions, indicating that planet–planet scattering is likely a more dominant mechanism than the Kozai–Lidov effect for TLGs. This was further supported by an anticorrelation trend found between planet multiplicity and eccentricity, as well as a lack of strong tidal dissipation effects for planets in our sample, which favour planet–planet scattering scenarios for the eccentricity origin.

ACKNOWLEDGEMENTS

We thank the referee for their thoughtful and helpful feedback, which helped improve the paper. AAQ acknowledges the funding bodies, the UAE Ministry of Presidential Affairs and the UAE Space Agency, for their support through the PhD scholarship. DK acknowledges MWGaiaDN, a Horizon Europe Marie Skłodowska-Curie Actions Doctoral Network funded under grant agreement no. 101072454 and also funded by UK Research and Innovation (EP/X031756/1). DK also acknowledges the UK's Science & Technology Facilities Council (STFC grant ST/W001136/1). YH was supported by JSPS KAKENHI grant number JP24H00017. IAS acknowledges the support of M.V. Lomonosov Moscow State University Program of Development. We thank Kento Masuda for the very helpful discussions on estimating the properties of the stellar parameters in this study. This research has made use of the Exoplanet Follow-up Observation Program (ExoFOP; DOI: 10.26134/ExoFOP5) website, which is operated by the California Institute of Technology, under contract with the National Aeronautics and Space Administration under the Exoplanet Exploration Program. This work has also made use of data from the European Space Agency (ESA) mission *Gaia* (<https://www.cosmos.esa.int/gaia>), processed by the *Gaia* Data Processing and Analysis Consortium (DPAC, <https://www.cosmos.esa.int/web/gaia/dpac/consortium>). Funding for the DPAC has been provided by national institutions, in particular the institutions participating in the *Gaia* Multilateral Agreement.

DATA AVAILABILITY

The data tables used and presented in this work are publicly available at CDS via anonymous ftp to <https://cdsarc.u-strasbg.fr> (130.79.128.5) or via <https://cdsarc.cds.unistra.fr/viz-bin/cat/J/MNRAS/539/307>. The coding scripts used for the analyses can be made available upon reasonable request.

REFERENCES

- Adibekyan V., 2019, *Geosci.*, 9, 105
Aerts C., 2021, *Rev. Mod. Phys.*, 93, 015001
Akeson R. L. et al., 2013, *PASP*, 125, 989
Almenara J. M. et al., 2015, *A&A*, 575, A71
Bach-Møller N., Jørgensen U. G., 2021, *MNRAS*, 500, 1313
Beaugé C., Nesvorný D., 2012, *ApJ*, 751, 119
Berger T. A., Huber D., Gaidos E., van Saders J. L., 2018, *ApJ*, 866, 99
Bitsch B., Kley W., 2010, *A&A*, 523, A30
Bitsch B., Trifonov T., Izidoro A., 2020, *A&A*, 643, A66
Bond J. C., Tinney C. G., Butler R. P., Jones H. R. A., Marcy G. W., Penny A. J., Carter B. D., 2006, *MNRAS*, 370, 163
Bonomo A. S. et al., 2017, *A&A*, 602, A107
Bowler B. P., Blunt S. C., Nielsen E. L., 2020, *AJ*, 159, 63
Brahm R. et al., 2023, *AJ*, 165, 227
Carrera D., Raymond S. N., Davies M. B., 2019, *A&A*, 629, L7
Chabrier G., Debras F., 2021, *ApJ*, 917, 4
Childs A. C., Quintana E., Barclay T., Steffen J. H., 2019, *MNRAS*, 485, 541
Davies M. et al., 2014, *Protostars and Planets VI*, Arizona Univ. Press, Tucson, p. 787
Dawson R. I., Murray-Clay R. A., 2013, *ApJ*, 767, L24
Debras F., Baruteau C., Donati J.-F., 2021, *MNRAS*, 500, 1621
, in Dhoubi H., Baruteau C., Mathis S., Debras F., Astoul A., Rieutord M., N'Diaye M., et al., 2023, eds, *SF2A-2023: Proceedings of the Annual meeting of the French Society of Astronomy and Astrophysics. Societe Francaise d'Astronomie et d'Astrophysique*, p. 373
Dressing C. D., Spiegel D. S., Scharf C. A., Menou K., Raymond S. N., 2010, *ApJ*, 721, 1295
El-Badry K., Rix H.-W., Heintz T. M., 2021, *MNRAS*, 506, 2269
Fabrycky D., Tremaine S., 2007, *ApJ*, 669, 1298
Fischer D. A., Valenti J., 2005, *ApJ*, 622, 1102
Ford E. B., Rasio F. A., 2008, *ApJ*, 686, 621
Fuhrmann K., Pfeiffer M. J., Bernkopf J., 1997, *A&A*, 326, 1081
Fuller J., Guillot T., Mathis S., Murray C., 2024, *Space Sci. Rev.*, 220, 22
Furlan E., Howell S. B., 2017, *AJ*, 154, 66
Furlan E., Howell S. B., 2020, *ApJ*, 898, 47
Gaia Collaboration, 2021, *A&A*, 649, A1
Gaia Collaboration, 2023, *A&A*, 674, A1
Gonzalez G., 1997, *MNRAS*, 285, 403
Haldemann J., Alibert Y., Mordasini C., Benz W., 2020, *A&A*, 643, A105
Hatzes A. P., 2016, *Space Sci. Rev.*, 205, 267
Hogg D. W., Myers A. D., Bovy J., 2010, *ApJ*, 725, 2166
Holman M., Touma J., Tremaine S., 1997, *Nature*, 386, 254
Ida S., Lin D. N. C., Nagasawa M., 2013, *ApJ*, 775, 42
Jackson B., Greenberg R., Barnes R., 2008, *ApJ*, 678, 1396
Jurić M., Tremaine S., 2008, *ApJ*, 686, 603
Kane S. R., Ciardi D. R., Gelino D. M., von Braun K., 2012, *MNRAS*, 425, 757
Kempton E. M. R. et al., 2018, *PASP*, 130, 114401
Knierim H., Shibata S., Helled R., 2022, *A&A*, 665, L5
Knutson H. A. et al., 2014, *ApJ*, 785, 126
Konatham S., Martin-Torres J., Zorzano M.-P., 2020, *Proc. R. Soc. Lond. Ser. A*, 476, 20200148
Lagrange A. M., Philipot F., Rubini P., Meunier N., Kiefer F., Kervella P., Delorme P., Beust H., 2023, *A&A*, 677, A71
Lainey V., Arlot J.-E., Karatekin Ö., van Hoolst T., 2009, *Nature*, 459, 957
Laws C., Gonzalez G., Walker K. M., Tyagi S., Dodsworth J., Snider K., Suntzeff N. B., 2003, *AJ*, 125, 2664
Lazovik Y. A., Barker A. J., de Vries N. B., Astoul A., 2024, *MNRAS*, 527, 8245
Levison H. F., Agnor C., 2003, *AJ*, 125, 2692
Lillo-Box J. et al., 2024, *A&A*, 686, A232
Limbach M. A., Turner E. L., 2015, *Proc. Natl. Acad. Sci.*, 112, 20
Lin D. N. C., Ida S., 1997, *ApJ*, 477, 781
Linsenmeier M., Pascale S., Lucarini V., 2015, *Planet. Space Sci.*, 105, 43
Mahmud M. M., Penev K. M., Schussler J. A., 2023, *MNRAS*, 525, 876
Mann C. R. et al., 2023, *AJ*, 166, 239
Masuda K., 2022, *ApJ*, 937, 94
Mathis S., 2018, in Deeg H. J., Belmonte J. A., eds, *Handbook of Exoplanets*. Springer Nature, p. 24
Méndez A., Rivera-Valentín E. G., 2017, *ApJ*, 837, L1
Nagasawa M., Ida S., 2011, *ApJ*, 742, 72
Nagasawa M., Ida S., Bessho T., 2008, *ApJ*, 678, 498
Naoz S., Farr W. M., Lithwick Y., Rasio F. A., Teyssandier J., 2011, *Nature*, 473, 187
Ngo H. et al., 2016, *ApJ*, 827, 8
Russell D. G., 2023, preprint ([arXiv:2303.06214](https://arxiv.org/abs/2303.06214))
Santos N. C., Israelian G., Mayor M., 2001, *A&A*, 373, 1019
Santos N. C., Israelian G., Mayor M., Rebolo R., Udry S., 2003, *A&A*, 398, 363
Seager S., Kuchner M., Hier-Majumder C. A., Militzer B., 2007, *ApJ*, 669, 1279
Shen Y., Turner E. L., 2008, *ApJ*, 685, 553
Shevchenko I. I., 2020, *The Lidov–Kozai Effect: Chaotic Implications*. Springer International Publishing, Cham, p. 325, https://doi.org/10.1007/978-3-030-52144-8_15
Silva Aguirre V. et al., 2015, *MNRAS*, 452, 2127
Swastik C., Banyal R. K., Narang M., Unni A., Banerjee B., Manoj P., Sivarani T., 2023, *AJ*, 166, 91
Trilling D. E., 2000, *ApJ*, 537, L61
Udry S., Santos N. C., 2007, *ARA&A*, 45, 397
Van Eylen V. et al., 2019, *AJ*, 157, 61
Villaver E., Livio M., Mustill A. J., Siess L., 2014, *ApJ*, 794, 3
Virtanen P. et al., 2020, *Nat. Methods*, 17, 261
Xie J.-W. et al., 2016, *Proc. Natl. Acad. Sci.*, 113, 11431
Zinzi A., Turrini D., 2017, *A&A*, 605, L4

APPENDIX A: NEXA PARAMETERS

Table A1. NEXA planet parameters of our target list that were used in our study.

TIC ID	Planet name	P (d)	σ_P (d)	R_p (R_{\oplus})	σ_{R_p} (R_{\oplus})	M_p (M_{\oplus})	σ_{M_p} (M_{\oplus})	e	σ_e	N
TIC 298663873	TOI-2180 b	260.79	0.58	11.32	0.23	875.62	26.70	0.368	0.007	1
TIC 172370679	TOI-1899 b	29.09031	0.000 04	11.10	0.34	212.95	12.71	0.04	0.03	1
TIC 377780790	Kepler-10 c	45.294 30	0.000 05	2.36	0.02	11.40	1.30	0.13	0.05	3
TIC 432254760	EPIC 249893012 c	15.624	0.001	3.67	0.15	14.67	1.86	0.07	0.06	3
TIC 73717937	HATS-17 b	16.254 61	0.000 07	8.71	0.63	425.26	20.66	0.03	0.02	1
TIC 377064495	TOI-561 d	25.7124	0.0001	2.82	0.07	13.20	0.95	0.12	0.05	4
TIC 377064495	TOI-561 e	77.03	0.24	2.55	0.12	12.60	1.40	0.08	0.05	4
TIC 264678534	HD 207897 b	16.202 16	0.000 08	2.50	0.08	14.40	1.60	0.05	0.04	1
TIC 332558858	TOI-2373 b	13.336 68	0.000 01	10.42	0.22	2955.80	63.57	0.112	0.008	1
TIC 441546821	HD 114082 b	109.75	0.39	11.21	0.34	2542.63	317.83	0.40	0.04	1
TIC 350618622	TOI-201 b	52.978 18	0.000 04	11.30	0.15	133.49	12.71	0.28	0.08	1
TIC 266593143	HAT-P-17 b	10.338 520	0.000 009	11.77	0.45	184.34	19.07	0.35	0.01	2
TIC 52368076	TOI-125 d	19.980	0.005	2.93	0.17	13.60	1.20	0.17	0.08	3
TIC 441739020	TOI-1670 c	40.7498	0.0001	11.06	0.28	200.23	27.02	0.09	0.04	2
TIC 273231214	KOI-94 e	54.3203	0.0001	6.56	0.62	35.00	23.00	0.02	0.23	4
TIC 120571842	Kepler-9 c	38.9853	0.0003	8.08	0.47	29.90	1.20	0.0669	0.0001	3
TIC 149601126	TOI-2525 c	49.2519	0.0004	10.13	0.11	208.81	10.01	0.157	0.008	2
TIC 358107516	TOI-2202 b	11.910	0.003	11.32	3.37	310.84	19.36	0.04	0.02	2
TIC 75878355	TOI-2134 c	95.50	0.30	7.27	0.42	41.89	7.76	0.67	0.06	2
TIC 157698565	TOI-2589 b	61.6277	0.0002	12.11	0.34	1112.40	31.78	0.522	0.006	1
TIC 68048686	K2-24 b	20.8898	0.0003	5.40	0.20	19.00	2.15	0.06	0.01	2
TIC 120571842	Kepler-9 b	19.238 91	0.000 06	8.29	0.48	43.40	1.80	0.061	0.001	3
TIC 275574174	KOI-3680 b	141.241 67	0.000 09	11.10	0.73	613.41	63.57	0.50	0.03	1
TIC 279741379	GJ 143 b	35.6125	0.0006	2.61	0.17	22.70	2.05	0.19	0.08	2
TIC 88992642	TOI-2145 b	10.2608	0.0008	11.98	0.32	1671.78	119.19	0.21	0.04	1
TIC 56815340	HD 106315 c	21.0570	0.0005	4.35	0.23	15.20	3.70	0.22	0.15	2
TIC 352682207	TOI-4010 d	14.708 86	0.000 03	6.18	0.14	38.15	3.25	0.07	0.03	4
TIC 219854519	TOI-4582 b	31.034	0.001	10.54	1.18	168.45	15.89	0.51	0.05	1
TIC 456862677	TOI-4515 b	15.266 45	0.000 01	12.17	0.43	637.00	17.00	0.461	0.007	1
TIC 299032847	Kepler-117 c	50.790 39	0.000 01	12.34	0.39	584.78	57.21	0.032	0.003	2
TIC 466206508	TOI-5542 b	75.1238	0.0002	11.31	0.40	419.53	31.78	0.02	0.02	1
TIC 237222864	HIP 97166 b	10.288 91	0.000 04	2.74	0.13	20.00	1.50	0.16	0.03	2
TIC 273231214	KOI-94 c	10.42365	0.00002	4.32	0.41	15.60	10.65	0.43	0.23	4
TIC 199376584	HD 332231 b	18.7120	0.0004	9.72	0.29	77.55	6.67	0.03	0.03	1
TIC 350020859	HD 89345 b	11.8143	0.0002	7.40	0.33	34.96	5.56	0.22	0.11	1
TIC 206541859	TOI-4406 b	30.083 64	0.000 05	11.21	0.22	95.35	9.53	0.15	0.04	1
TIC 24358417	TOI-2338 b	22.653 98	0.000 02	11.21	0.22	1900.61	65.15	0.676	0.002	1
TIC 405010127	CoRoT-10 b	13.2406	0.0002	10.87	0.78	874.00	50.85	0.53	0.04	1
TIC 166739520	WASP-117 b	10.0216	0.0006	11.88	0.79	95.35	15.89	0.30	0.02	1
TIC 445805961	TOI-1710 b	24.283 38	0.000 02	5.15	0.12	18.40	4.65	0.18	0.11	1
TIC 302773669	HD 17156 b	21.2166	0.0004	12.33	0.34	1115.58	66.74	0.68	0.00	1
TIC 120960812	Kepler-25 c	12.7207	0.0001	5.22	0.07	15.20	1.45	0.006	0.004	3
TIC 279401253	TIC 279401253 b	76.80	0.06	11.21	0.45	1951.47	128.72	0.45	0.03	2
TIC 209464063	TOI-5678 b	47.7302	0.0001	4.91	0.08	20.00	4.00	0.14	0.07	1
TIC 304142124	HD 95338 b	55.09	0.02	3.89	0.20	42.44	2.15	0.20	0.03	1
TIC 394137592	HD 1397 b	11.5353	0.0008	11.50	0.29	131.90	6.36	0.25	0.02	1
TIC 94986319	TOI-421 c	16.0682	0.0004	5.09	0.15	16.42	1.05	0.15	0.04	2
TIC 273231214	KOI-94 d	22.342 989	0.000 007	11.27	1.06	106.00	11.00	0.02	0.04	4
TIC 280206394	TOI-677 b	11.2366	0.0001	13.12	0.34	392.84	21.61	0.44	0.02	1
TIC 7020254	K2-115 b	20.2726	0.0003	12.06	0.22	266.98	60.39	0.14	0.07	1
TIC 281885301	K2-19 c	11.8993	0.0008	4.10	0.20	10.80	0.60	0.21	0.03	3
TIC 339672028	TOI-481 b	10.331 11	0.000 02	11.10	0.11	486.28	9.53	0.153	0.006	1
TIC 281731203	K2-261 b	11.633 48	0.000 02	9.53	0.39	59.75	7.95	0.29	0.07	1
TIC 68577662	K2-232 b	11.168 45	0.000 02	11.21	0.24	126.50	11.76	0.26	0.02	1
TIC 409794137	TOI-1478 b	10.180 25	0.000 02	11.88	0.44	270.47	15.73	0.02	0.02	1
TIC 353459965	HAT-P-15 b	10.863 50	0.000 03	11.88	0.79	616.59	95.35	0.19	0.02	1
TIC 343019899	TOI-1386 b	25.8384	0.0001	6.05	0.19	47.04	5.88	0.06	0.05	2
TIC 349486888	HD 152843 b	11.626	0.002	3.41	0.13	11.56	6.36	0.14	0.17	2
TIC 26547036	TOI-2010 b	141.834 02	0.000 07	11.81	0.30	408.73	17.80	0.21	0.02	1

Table A1 – continued

TIC ID	Planet name	P (d)	σ_P (d)	R_p (R_{\oplus})	σ_{R_p} (R_{\oplus})	M_p (M_{\oplus})	σ_{M_p} (M_{\oplus})	e	σ_e	N
TIC 163539739	TOI-1278 b	14.4757	0.0002	12.22	2.47	5879.83	158.91	0.013	0.004	1
TIC 149601126	TOI-2525 b	23.286	0.002	8.68	0.11	26.70	1.59	0.17	0.01	2
TIC 301258470	K2-329 b	12.455 122	0.0000 03	8.68	0.28	82.64	6.67	0.07	0.04	1
TIC 120255950	Kepler-1656 b	31.56	0.01	4.52	0.52	47.80	4.75	0.84	0.04	2
TIC 432254760	EPIC 249893012 d	35.747	0.005	3.94	0.12	10.18	2.44	0.15	0.16	3
TIC 54002556	NGTS-11 b	35.4553	0.0002	9.16	0.34	109.33	26.22	0.13	0.10	1
TIC 237913194	TIC 237913194 b	15.168 86	0.000 02	12.52	0.57	617.23	29.08	0.57	0.01	1
TIC 309792357	TOI-199 b	104.854	0.002	9.08	0.06	54.03	6.36	0.09	0.02	2
TIC 366576758	K2-114 b	11.390 931	0.000 003	10.45	0.35	638.84	38.14	0.08	0.03	1
TIC 130162252	CoRoT-9 b	95.27266	0.000 07	11.95	0.77	266.98	15.89	0.13	0.04	1
TIC 350738167	Kepler-1704 b	988.8811	0.0009	11.95	0.48	1322.17	90.58	0.92	0.01	1
TIC 124029677	TOI-5153 b	20.330 03	0.000 07	11.88	0.45	1036.12	55.62	0.09	0.02	1
TIC 207110080	TOI-558 b	14.574 07	0.000 03	12.17	0.44	1147.36	47.67	0.30	0.02	1
TIC 176966903	K2-99 b	18.252	0.001	11.73	0.42	308.30	28.60	0.19	0.04	1
TIC 363573185	K2-10 b	19.304	0.001	3.84	0.34	27.00	16.50	0.31	0.17	1
TIC 257527578	NGTS-20 b	54.1892	0.0001	11.99	0.45	947.13	49.26	0.43	0.02	1
TIC 73848324	K2-287 b	14.893 29	0.000 02	9.49	0.15	100.12	8.58	0.48	0.03	1
TIC 137685450	Kepler-1514 b	217.8318	0.0001	12.42	0.26	1678.14	69.92	0.40	0.01	2
TIC 27454084	Kepler-419 b	69.7546	0.0008	10.80	1.35	794.50	95.30	0.83	0.01	2
TIC 447061717	TOI-1231 b	24.245 59	0.000 07	3.65	0.15	15.40	3.30	0.09	0.09	1
TIC 270611401	Kepler-434 b	12.874 710	0.000 005	12.67	2.46	908.96	111.24	0.13	0.07	1
TIC 298969838	Kepler-413 b	66.26	0.02	4.35	0.10	67.00	21.50	0.118	0.002	1
TIC 457134360	HD 80606 b	111.4367	0.0004	11.99	0.34	1392.10	235.19	0.93	0.00	1
TIC 141488193	TOI-4127 b	56.3988	0.0001	12.29	0.40	731.01	34.96	0.747	0.008	1
TIC 272836943	Kepler-39 b	21.087 21	0.000 04	13.90	1.06	6388.10	397.30	0.11	0.06	1
TIC 11023038	K2-139 b	28.3806	0.0005	9.11	0.17	123.00	25.11	0.12	0.10	1
TIC 441462736	HD 221416 b	14.277	0.004	9.17	0.33	60.50	5.70	0.12	0.03	1
TIC 159311390	Kepler-643 b	16.338 90	0.000 02	10.16	0.31	321.01	63.57	0.37	0.06	1
TIC 159647910	KOI-1257 b	86.647 66	0.000 03	10.54	1.35	460.83	111.24	0.77	0.04	1
TIC 150098860	TOI-220 b	10.695 26	0.000 09	3.03	0.15	13.80	1.00	0.03	0.03	1
TIC 743941	K2-292 b	16.9841	0.0008	2.63	0.10	24.50	4.40	0.04	0.04	1
TIC 97568467	TOI-2497 b	10.655 67	0.000 04	11.14	0.58	1531.93	130.31	0.20	0.04	1
TIC 1042868	HD 88986 b	146.05	0.41	2.49	0.18	17.20	3.90	0.24	0.05	1

Table A2. NEXA stellar parameters of our target list that were used in our study. Missing values are denoted with ‘-’.

TIC ID	Host Name	Age (Gyr)	σ_{Age} (Gyr)	[Fe/H]	$\sigma_{[\text{Fe}/\text{H}]}$	$T_{\text{eff},*}$ (K)	$\sigma_{T_{\text{eff},*}}$ (K)	K (mag)	σ_K (mag)
TIC 298663873	TOI-2180	8.10	1.40	0.25	0.06	5695	59	7.60	0.02
TIC 172370679	TOI-1899	7.10	4.65	0.28	0.11	3926	46	10.51	0.02
TIC 377780790	Kepler-10	10.60	1.40	-0.15	0.04	5708	28	9.50	0.02
TIC 432254760	EPIC 249893012	9.00	0.55	0.20	0.05	5430	85	9.71	0.02
TIC 73717937	HATS-17	2.10	1.30	0.30	0.03	5846	78	10.70	0.02
TIC 377064495	TOI-561	11.00	3.15	-0.40	0.05	5372	70	8.39	0.02
TIC 264678534	HD 207897	7.10	4.50	-0.04	0.04	5070	58	6.31	0.03
TIC 332558858	TOI-2373	5.90	1.70	0.30	0.05	5651	80	11.59	0.02
TIC 441546821	HD 114082	0.015	0.006	0.00	0.03	6651	35	7.16	0.03
TIC 350618622	TOI-201	0.87	0.47	0.24	0.04	6394	75	7.85	0.02
TIC 266593143	HAT-P-17	7.80	3.30	0.00	0.08	5246	80	8.54	0.02
TIC 52368076	TOI-125	6.80	4.25	-0.02	0.03	5320	39	8.99	0.02
TIC 441739020	TOI-1670	2.53	0.43	0.09	0.07	6170	61	8.72	0.02
TIC 273231214	KOI-94	3.16	0.39	0.023	0.002	6182	58	10.93	0.02
TIC 120571842	Kepler-9	2.00	1.65	0.05	0.07	5774	60	12.34	0.02
TIC 149601126	TOI-2525	3.99	3.45	0.14	0.05	5096	102	11.90	0.02
TIC 358107516	TOI-2202	7.48	3.33	0.04	0.05	5144	50	10.80	0.02
TIC 75878355	TOI-2134	3.80	4.10	0.12	0.02	4580	50	6.09	0.02
TIC 157698565	TOI-2589	11.00	2.00	0.12	0.04	5579	70	9.63	0.02
TIC 68048686	K2-24	5.10	1.90	0.34	0.04	5625	60	9.18	0.02
TIC 275574174	KOI-3680	3.20	5.95	0.16	0.07	5830	100	13.10	0.04
TIC 279741379	GJ 143	3.80	3.70	0.003	0.060	4640	100	5.38	0.02

Table A2 – *continued*

TIC ID	Host Name	Age (Gyr)	σ_{Age} (Gyr)	[Fe/H]	$\sigma_{[\text{Fe}/\text{H}]}$	$T_{\text{eff},\star}$ (K)	$\sigma_{T_{\text{eff},\star}}$ (K)	K (mag)	σ_K (mag)
TIC 88992642	TOI-2145	1.80	0.28	0.25	0.07	6177	67	7.76	0.03
TIC 56815340	HD 106315	4.48	0.96	-0.31	0.08	6327	48	7.85	0.02
TIC 352682207	TOI-4010	6.10	3.10	0.37	0.07	4960	36	10.16	0.02
TIC 219854519	TOI-4582	4.00	1.00	0.17	0.06	5190	100	9.33	0.02
TIC 456862677	TOI-4515	1.20	0.20	0.05	0.03	5433	70	10.13	0.02
TIC 299032847	Kepler-117	5.30	1.40	-0.04	0.10	6150	110	13.01	0.03
TIC 466206508	TOI-5542	10.80	2.85	-0.21	0.08	5700	80	10.90	0.02
TIC 237222864	HIP 97166	3.33	3.28	0.27	0.09	5198	100	7.92	0.02
TIC 199376584	HD 332231	4.30	2.20	0.04	0.06	6089	96	7.24	0.02
TIC 350020859	HD 89345	7.53	1.15	0.42	0.05	5576	74	7.72	0.02
TIC 206541859	TOI-4406	2.90	0.70	0.10	0.05	6219	70	9.73	0.02
TIC 24358417	TOI-2338	7.00	2.00	0.22	0.04	5581	60	10.66	0.02
TIC 405010127	CoRoT-10	3.0	-	0.26	0.07	5075	75	11.78	0.02
TIC 166739520	WASP-117	4.60	2.00	-0.11	0.14	6040	90	8.78	0.02
TIC 445805961	TOI-1710	2.80	0.60	0.12	0.06	5730	30	7.96	0.03
TIC 302773669	HD 17156	3.37	0.33	0.24	0.03	6040	24	6.76	0.02
TIC 120960812	Kepler-25	2.75	0.30	0.11	0.03	6354	27	9.49	0.02
TIC 279401253	TIC 279401253	1.20	0.90	0.20	0.05	5951	80	10.34	0.02
TIC 209464063	TOI-5678	8.50	3.00	0.00	0.01	5485	63	9.56	0.02
TIC 304142124	HD 95338	5.08	2.51	0.04	0.10	5212	13	6.59	0.02
TIC 394137592	HD 1397	4.51	0.50	0.29	0.09	5521	60	5.99	0.02
TIC 94986319	TOI-421	9.40	2.75	-0.02	0.05	5325	68	8.07	0.02
TIC 280206394	TOI-677	2.92	0.77	0.00	0.05	6295	77	8.43	0.02
TIC 7020254	K2-115	10.70	2.95	-0.10	0.05	5657	60	11.72	0.02
TIC 281885301	K2-19	8.0	-	0.06	0.05	5322	100	11.16	0.03
TIC 339672028	TOI-481	6.70	0.50	0.26	0.05	5735	72	8.44	0.02
TIC 281731203	K2-261	9.30	1.80	0.36	0.06	5445	76	8.89	0.02
TIC 68577662	K2-232	1.43	0.78	0.10	0.04	6154	60	8.43	0.02
TIC 409794137	TOI-1478	9.10	3.50	0.08	0.07	5597	82	9.20	0.02
TIC 353459965	HAT-P-15	6.80	2.05	0.22	0.08	5568	90	9.64	0.02
TIC 343019899	TOI-1386	3.30	2.85	0.16	0.06	5793	74	9.09	0.02
TIC 349488688	HD 152843	3.97	0.75	-0.16	0.05	6310	100	7.63	0.02
TIC 26547036	TOI-2010	1.90	1.75	0.17	0.06	5929	74	8.28	0.02
TIC 163539739	TOI-1278	-	-	-0.01	0.28	3799	42	9.74	0.01
TIC 301258470	K2-329	1.80	1.75	0.10	0.07	5282	39	10.67	0.02
TIC 120255950	Kepler-1656	6.31	2.50	0.19	0.04	5569	50	9.64	0.02
TIC 54002556	NGTS-11	3.90	1.60	0.22	0.08	5050	80	10.32	0.02
TIC 237913194	TIC 237913194	5.70	1.70	0.14	0.05	5788	80	10.48	0.02
TIC 309792357	TOI-199	0.80	0.90	0.22	0.03	5255	11	8.81	0.02
TIC 366576758	K2-114	7.20	4.40	0.41	0.04	4920	68	12.30	0.03
TIC 130162252	CoRoT-9	6.00	3.00	-0.01	0.06	5625	80	11.69	0.02
TIC 350738167	Kepler-1704	7.40	1.25	0.20	0.06	5746	87	11.79	0.03
TIC 124029677	TOI-5153	5.40	1.00	0.12	0.08	6300	80	10.41	0.02
TIC 207110080	TOI-558	1.79	0.82	-0.004	0.057	6466	94	10.26	0.02
TIC 176966903	K2-99	2.40	0.40	0.21	0.06	6217	78	9.72	0.02
TIC 363573185	K2-10	-	-	-0.07	0.07	5620	70	10.64	0.02
TIC 257527578	NGTS-20	4.10	2.70	0.15	0.08	5980	80	9.83	0.02
TIC 73848324	K2-287	4.50	1.00	0.20	0.04	5695	58	9.19	0.02
TIC 137685450	Kepler-1514	2.90	1.45	0.12	0.08	6145	89	10.69	0.02
TIC 27454084	Kepler-419	1.29	0.25	0.18	0.07	6430	79	11.86	0.02
TIC 447061717	TOI-1231	-	-	0.04	0.07	3553	51	8.07	0.03
TIC 270611401	Kepler-434	4.00	1.70	0.25	0.14	5977	95	13.04	0.03
TIC 298969838	Kepler-413	-	-	-1.44	0.30	4717	145	13.42	0.04
TIC 457134360	HD 80606	5.90	1.80	0.34	0.05	5561	24	7.32	0.02
TIC 141488193	TOI-4127	4.80	2.10	0.14	0.12	6096	115	10.24	0.02
TIC 272836943	Kepler-39	2.10	0.85	0.10	0.14	6350	100	12.92	0.03
TIC 11023038	K2-139	1.80	0.30	0.24	0.05	5370	68	9.66	0.02
TIC 441462736	HD 221416	4.90	1.10	-0.08	0.08	5080	90	6.04	0.02
TIC 159311390	Kepler-643	12.02	2.05	0.13	0.09	4908	46	11.58	0.01
TIC 159647910	KOI-1257	9.30	3.00	0.27	0.09	5520	80	12.73	0.02
TIC 150098860	TOI-220	10.10	1.40	-0.22	0.04	5298	65	8.54	0.02
TIC 743941	K2-292	6.80	2.30	0.07	0.05	5725	65	8.41	0.03
TIC 97568467	TOI-2497	1.00	0.20	0.09	0.07	7360	310	8.49	0.02
TIC 1042868	HD 88986	7.90	1.30	0.06	0.02	5861	17	4.88	0.02

APPENDIX B: JAXSTAR PARAMETERS

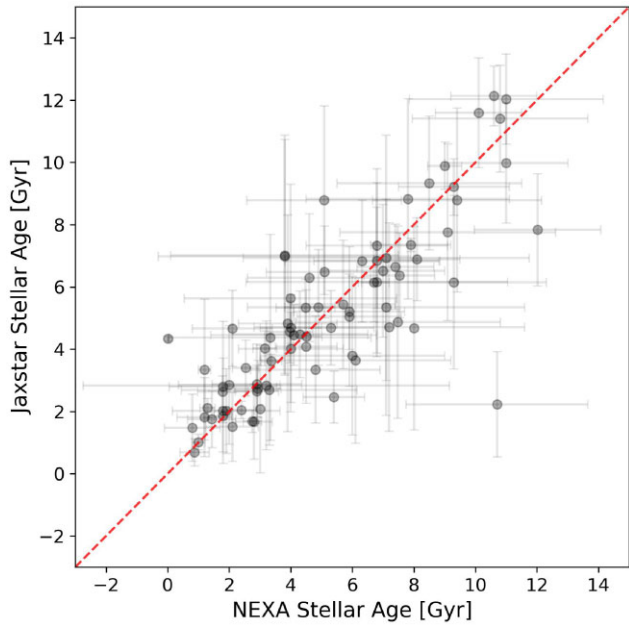


Figure B1. NEXA versus JAXSTAR-derived stellar ages.

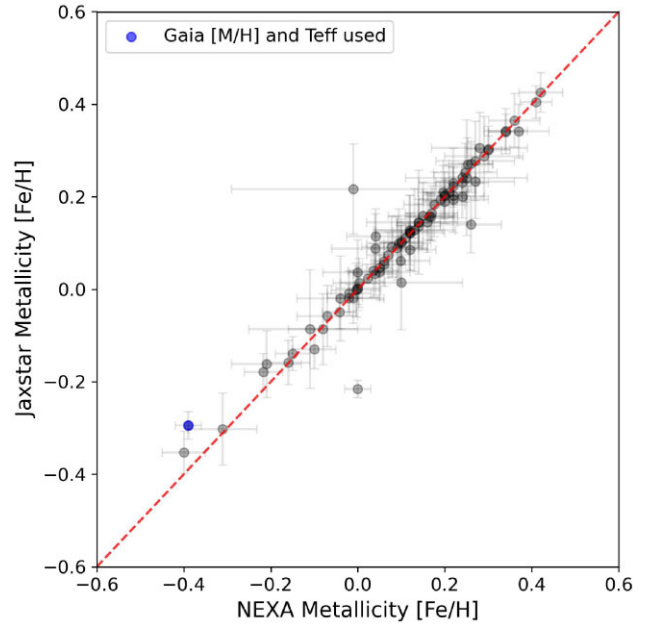


Figure B2. NEXA versus JAXSTAR-derived stellar metallicities.

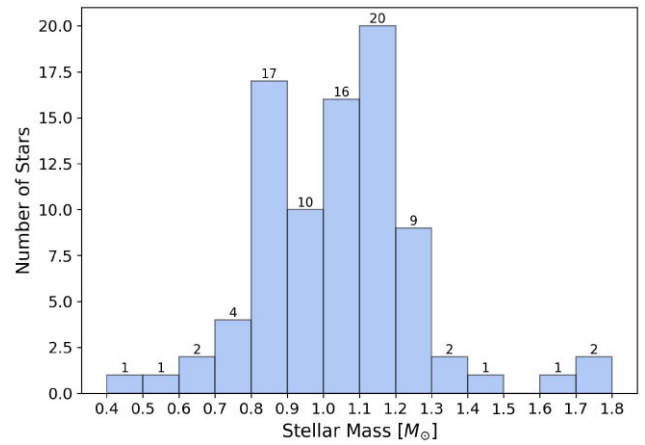


Figure B3. Distribution of JAXSTAR-derived stellar masses for the host stars in our sample.

Downloaded from https://academic.oup.com/mnras/article/539/1/307/8071980 by guest on 19 May 2025

Table B1. Homogenously derived stellar parameters using JAXSTAR for the host stars of our sample.

TIC ID	Age (Gyr)	σ_{Age} (Gyr)	[Fe/H]	$\sigma_{[\text{Fe}/\text{H}]}$	M_{\star} (M_{\odot})	$\sigma_{M_{\star}}$ (M_{\odot})	R_{\star} (R_{\odot})	$\sigma_{R_{\star}}$ (R_{\odot})	$T_{\text{eff},\star}$ (K)	$\sigma_{T_{\text{eff},\star}}$ (K)
TIC 339672028	6.15	1.28	0.27	0.05	1.19	0.06	1.65	0.02	5757	67
TIC 94986319	8.79	2.95	-0.009	0.048	0.85	0.03	0.867	0.009	5343	59
TIC 273231214	4.02	0.56	0.023	0.002	1.15	0.02	1.35	0.02	6177	58
TIC 199376584	4.48	1.39	0.04	0.06	1.11	0.05	1.26	0.02	6092	97
TIC 281885301	4.68	3.27	0.05	0.05	0.88	0.03	0.83	0.01	5283	73
TIC 266593143	8.83	3.21	0.04	0.07	0.85	0.03	0.86	0.01	5282	63
TIC 377064495	12.03	1.44	-0.35	0.05	0.77	0.01	0.829	0.007	5506	39
TIC 350020859	6.37	1.36	0.43	0.04	1.21	0.07	1.72	0.02	5615	80
TIC 409794137	7.76	2.84	0.09	0.07	0.95	0.05	1.01	0.01	5614	77
TIC 166739520	6.30	2.05	-0.09	0.13	1.03	0.07	1.23	0.02	6047	89
TIC 280206394	2.73	0.91	0.002	0.049	1.17	0.04	1.27	0.02	6298	76
TIC 56815340	5.34	0.89	-0.30	0.08	1.03	0.04	1.27	0.01	6328	47
TIC 7020254	2.23	1.69	-0.13	0.04	0.91	0.02	0.842	0.009	5612	46
TIC 68577662	1.75	0.91	0.10	0.04	1.17	0.03	1.17	0.01	6151	56
TIC 302773669	3.62	0.22	0.24	0.03	1.27	0.01	1.52	0.02	6040	24
TIC 350618622	0.68	0.44	0.23	0.03	1.32	0.02	1.30	0.01	6352	54
TIC 281731203	9.21	0.91	0.36	0.06	1.10	0.03	1.66	0.02	5458	77
TIC 73717937	4.67	1.22	0.30	0.03	1.16	0.03	1.29	0.02	5847	79
TIC 353459965	6.84	2.96	0.23	0.08	1.00	0.05	1.04	0.01	5580	84
TIC 52368076	6.16	2.40	-0.02	0.03	0.86	0.02	0.835	0.009	5320	39
TIC 332558858	5.05	2.24	0.30	0.05	1.06	0.04	1.09	0.02	5660	79
TIC 377780790	12.13	0.96	-0.14	0.04	0.87	0.02	1.07	0.01	5714	25
TIC 432254760	9.89	0.76	0.20	0.05	1.06	0.02	1.71	0.03	5443	84
TIC 264678534	5.35	3.48	-0.05	0.04	0.80	0.03	0.763	0.009	5053	46
TIC 441546821	4.33	0.07	-0.22	0.02	1.148	0.008	1.56	0.02	6439	25
TIC 149601126	5.64	3.66	0.14	0.05	0.85	0.03	0.809	0.010	5064	63
TIC 441739020	3.39	0.89	0.09	0.07	1.17	0.04	1.31	0.01	6169	60
TIC 358107516	4.87	3.09	0.03	0.05	0.84	0.03	0.798	0.009	5131	44
TIC 456862677	3.34	2.26	0.05	0.03	0.91	0.03	0.853	0.009	5409	52
TIC 75878355	6.98	3.76	0.12	0.02	0.75	0.02	0.714	0.005	4587	30
TIC 68048686	6.48	1.48	0.34	0.04	1.06	0.03	1.14	0.01	5626	58
TIC 157698565	9.98	1.93	0.12	0.04	0.95	0.03	1.09	0.01	5595	62
TIC 275574174	2.83	2.07	0.14	0.07	1.06	0.04	1.02	0.02	5787	79
TIC 279741379	7.02	3.86	0.01	0.05	0.74	0.02	0.708	0.007	4674	53
TIC 88992642	1.86	0.22	0.25	0.06	1.70	0.05	2.76	0.04	6176	62
TIC 352682207	3.64	2.66	0.34	0.06	0.88	0.02	0.813	0.007	4946	31
TIC 219854519	4.68	0.50	0.16	0.06	1.30	0.04	2.48	0.04	5166	103
TIC 237222864	4.38	3.31	0.23	0.08	0.90	0.03	0.836	0.009	5118	66
TIC 299032847	4.68	1.19	-0.02	0.09	1.18	0.07	1.57	0.04	6155	102
TIC 466206508	11.41	1.71	-0.16	0.07	0.88	0.03	1.07	0.01	5757	61
TIC 445805961	1.67	1.20	0.09	0.05	1.02	0.03	0.95	0.01	5720	27
TIC 206541859	2.65	0.84	0.10	0.05	1.20	0.04	1.29	0.02	6220	69
TIC 24358417	6.52	2.13	0.22	0.04	1.00	0.03	1.04	0.01	5585	59
TIC 405010127	2.08	2.05	0.14	0.06	0.83	0.02	0.759	0.008	4886	53
TIC 120571842	2.85	1.90	0.04	0.06	1.00	0.04	0.96	0.01	5762	53
TIC 120960812	1.69	0.36	0.11	0.03	1.25	0.02	1.31	0.01	6354	27
TIC 279401253	1.82	1.27	0.19	0.05	1.12	0.03	1.09	0.01	5913	61
TIC 209464063	9.34	2.15	0.0001	0.0099	0.88	0.02	0.93	0.01	5498	59
TIC 304142124	8.78	3.03	0.09	0.08	0.86	0.04	0.857	0.007	5212	13
TIC 394137592	4.41	0.10	0.29	0.09	1.34	0.02	2.36	0.03	5525	61
TIC 172370679	6.94	3.94	0.31	0.08	0.63	0.01	0.601	0.004	3934	29
TIC 343019899	2.70	1.78	0.16	0.05	1.06	0.04	1.02	0.01	5774	62
TIC 349488688	4.56	0.99	-0.16	0.05	1.12	0.04	1.41	0.02	6308	94
TIC 26547036	2.01	1.36	0.16	0.05	1.11	0.04	1.070	0.010	5906	59
TIC 163539739	6.91	3.98	0.22	0.10	0.564	0.009	0.533	0.004	3807	37
TIC 301258470	2.80	2.10	0.06	0.05	0.89	0.02	0.820	0.009	5265	36
TIC 120255950	6.83	1.96	0.19	0.04	0.98	0.03	1.02	0.01	5572	49
TIC 298663873	6.89	1.34	0.27	0.06	1.16	0.06	1.60	0.01	5716	59
TIC 54002556	4.83	3.48	0.19	0.07	0.86	0.03	0.805	0.009	5006	58
TIC 237913194	5.44	2.06	0.14	0.05	1.04	0.04	1.11	0.01	5794	79
TIC 309792357	1.48	1.08	0.20	0.02	0.94	0.01	0.845	0.007	5252	10
TIC 366576758	4.71	3.35	0.40	0.04	0.88	0.03	0.81	0.01	4887	49
TIC 130162252	3.80	2.55	-0.02	0.05	0.93	0.04	0.89	0.01	5605	64

Table B1 – continued

TIC ID	Age (Gyr)	σ_{Age} (Gyr)	[Fe/H]	$\sigma_{[\text{Fe}/\text{H}]}$	M_{\star} (M_{\odot})	$\sigma_{M_{\star}}$ (M_{\odot})	R_{\star} (R_{\odot})	$\sigma_{R_{\star}}$ (R_{\odot})	$T_{\text{eff},\star}$ (K)	$\sigma_{T_{\text{eff},\star}}$ (K)
TIC 350738167	6.64	1.37	0.21	0.06	1.16	0.06	1.64	0.03	5771	86
TIC 124029677	2.46	0.84	0.12	0.08	1.25	0.05	1.38	0.02	6300	81
TIC 207110080	2.63	0.51	−0.002	0.058	1.28	0.04	1.53	0.02	6466	96
TIC 176966903	2.05	0.28	0.21	0.06	1.62	0.05	2.52	0.04	6211	73
TIC 363573185	6.98	2.97	−0.06	0.07	0.91	0.04	0.93	0.01	5630	65
TIC 257527578	4.46	0.97	0.16	0.07	1.26	0.07	1.75	0.02	5984	72
TIC 73848324	4.08	1.82	0.20	0.04	1.04	0.03	1.03	0.01	5697	56
TIC 137685450	2.88	1.28	0.13	0.08	1.18	0.05	1.27	0.02	6154	89
TIC 27454084	2.11	0.31	0.18	0.07	1.44	0.04	1.79	0.03	6430	79
TIC 447061717	7.46	3.81	0.11	0.06	0.473	0.007	0.445	0.005	3661	25
TIC 270611401	4.02	1.74	0.24	0.13	1.18	0.07	1.32	0.04	5973	95
TIC 298969838	12.59	1.20	−0.29	0.03	0.683	0.008	0.687	0.007	4925	19
TIC 457134360	5.20	1.21	0.34	0.05	1.04	0.02	1.05	0.01	5561	23
TIC 141488193	3.34	1.72	0.14	0.11	1.17	0.07	1.26	0.02	6092	109
TIC 272836943	1.50	1.11	0.01	0.10	1.18	0.05	1.19	0.02	6303	89
TIC 11023038	2.02	1.69	0.20	0.05	0.94	0.02	0.854	0.008	5278	47
TIC 441462736	5.34	1.86	−0.09	0.08	1.21	0.11	2.90	0.04	5054	82
TIC 159311390	7.83	1.80	0.13	0.09	1.13	0.08	2.56	0.04	4903	44
TIC 159647910	6.15	2.78	0.28	0.09	1.28	0.23	2.21	0.77	5532	81
TIC 150098860	11.59	1.76	−0.18	0.04	0.80	0.02	0.841	0.009	5387	43
TIC 743941	7.33	2.02	0.07	0.05	0.98	0.04	1.07	0.02	5730	64
TIC 97568467	1.02	0.25	0.10	0.07	1.79	0.08	2.22	0.05	7341	322
TIC 1042868	7.35	0.22	0.06	0.02	1.09	0.01	1.58	0.01	5860	16

This paper has been typeset from a $\text{\TeX}/\text{\LaTeX}$ file prepared by the author.